

ARTICLE

AVEIRO - PORTUGAL



This paper must be cited as:

Shi, R., Martínez, E. D., Brites, C. D. S., Carlos, L. D., Phys. Chem. Chem. Phys., 2021,23, 20-42. <https://doi.org/10.1039/D0CP05069E>

Received 00th January 20xx,
Accepted 00th January 20xx

DOI: 10.1039/x0xx00000x

Thermal enhancement of upconversion emission in nanocrystals: a comprehensive summary

Rui Shi,^{*a} Eduardo D. Martinez,^b Carlos D. S. Brites^a and Luís D. Carlos^{*a}

Luminescence thermal stability is a major figure of merit of lanthanide-doped nanoparticles playing an essential role in determining their potential applications in advanced optics. Unfortunately, considering the intensification of multiple electron-vibration interactions as temperature increases, luminescence thermal quenching of material is generally considered to be inevitable. Recently, the emergence of thermally enhanced upconversion luminescence in lanthanide-doped nanoparticles seemed to challenge this stereotype, and the research on this topic rapidly aroused wide attention. While considerable efforts have been made to explore the origin of this phenomenon, the key mechanism of luminescence enhancement is still under debate. Here, to sort out the context of this intriguing finding, the reported results on this exciting topic are reviewed, and the corresponding enhancement mechanisms as proposed by different researchers are summarized. Detailed analyses are provided to evaluate the contribution of most believed “surface-attached moisture desorption” process on the overall luminescence enhancement at elevated temperatures. The impacts of other surface-related processes and shell passivation on the luminescence behaviour of the materials are also elaborated. The lack of standardization in the reported data and the absence of important experimental information, which greatly puzzle the results cross-checking and reanalysis, is emphasized as well. On the foundation of these discussions, it is realized that the thermal-induced luminescence enhancement is a form of recovery process against the strong luminescence quenching in the system, and the enhancement degree is closely associated with the extent of luminescence loss induced by various quenching effects beforehand.

Introduction

Photon upconversion, involving the sequential absorption of two or more low-energy photons leading to the emission of light at a shorter wavelength, had attracted great attention in the last decades.¹⁻⁵ Different from early reported upconversion phenomena, as second-harmonic generation⁶ and two-photon absorption,⁷ which could be only triggered by high-power excitation sources, nowadays photon upconversion is easily achieved in lanthanide-doped inorganic materials by employing a commercial low power-density laser or even a near-infrared light-emitting diode lamp.⁸ Due to the ladder-like 4f level structures of trivalent lanthanide ions (Ln³⁺) and the relatively long lifetimes of their excited states, two or more low-energy excitation photons are absorbed successively, leading to the stepwise pumping of electrons into upper excited states, resulting in the high-energy radiative emission. Besides, the creative concept of “energy transfer (ET) upconversion” as proposed by Auzel^{9, 10} introduced the critical role of sensitizer ions (such as Yb³⁺ and Nd³⁺) owning the efficient absorption of excitation photons into the system. This strategy for surpassing the constraint of insufficient light absorptivity of the activator ions (such as Er³⁺, Tm³⁺ and Ho³⁺) greatly enhances the upconversion luminescence (UCL) intensity of materials.¹¹ Started from the beginning of this century, the rapid progress of nanotechnology has brought new opportunities and challenges to develop nanosized materials with high UCL

efficiency. The control on spatial distributions of different dopants in the nanoparticles (NPs) has been realized as an effective way to modulate the involved ET pathway and further boost the luminescence intensity of the materials.¹²⁻¹⁴ One illustrative example is the successful development of core-shell Ln³⁺-doped upconversion NPs (UCNPs) with the activator and sensitizer ions localized in different regions (i.e. in the core or shell of the NPs).¹⁵ Because of these remarkable improvements, Ln³⁺-doped UCNPs have been widely applied in various fields, such as bioimaging,¹⁶ anti-counterfeiting,¹⁷ holography,¹⁸ near-field microscopies,¹⁹ and local temperature monitoring.²⁰ Despite these great achievements, the fairly low UCL quantum yield (QY) of NPs is still one of the main drawbacks restricting their practical application.^{21, 22} For example, Yb³⁺/Er³⁺ co-doped β -NaYF₄, one of the most used UCNPs presents an upconversion QY typically less than 1% upon 980 nm commercial laser excitation,²³ which is far from the QY value (~10%) of its bulk form.²⁴ Given the identical crystal structure, site occupancy, and doping concentration of these two forms, surface-related processes are believed as the major factor behind this huge difference in the luminescence performance (the relaxation of transition selection rules, which plays a vital role in controlling the 4f-4f luminescence properties, is also similar in both cases). As one of the unique features of NPs, the large surface-to-volume ratio (SVR) makes the luminescence properties more sensitive to the particle surface. Considering the nonlinearity of the upconversion process, a minor effect of the surface-related quenching on the primary transition of the sensitizer ions will have a great impact on the subsequently high-order UCL properties of the activators in the NP.

Recently, the topic of thermally enhanced UCL has attracted considerable attention^{25, 26} (although no monograph review has yet been published). Several groups reported an enhancement of the UCL of Ln³⁺-doped NPs as temperature increased from room temperature (RT) to high temperatures (420-470 K),²⁷⁻²⁹

^a Phantom-g, CICECO-Aveiro Institute of Materials, Physics Department, University of Aveiro, 3810-193 Aveiro, Portugal.

^b Instituto de Nanociencia y Nanotecnología (INN), Centro Atómico Bariloche, Comisión Nacional de Energía Atómica (CNEA), Consejo Nacional de Investigaciones Científicas y Técnicas (CONICET), Av. E. Bustillo 9500, R8402AGP San Carlos de Bariloche, Río Negro, Argentina.

† E-mail: ruishi@ua.pt and lcarlos@ua.pt

which contradicted the well-known and conventional luminescence thermal quenching.³⁰ Although substantial experimental results have been reported in the past 15 years, the mechanism underpinning this phenomenon is still under debate. Heat is commonly considered to have a negative effect on the luminescence performance of optical materials and de-excitation processes (e.g., thermal-induced ionization,³¹ multiphonon relaxation,³² and electron transfer³³) are efficiently promoted at high temperatures leading to a strong luminescence thermal quenching of individual centres. For the multiple ET-based processes, such as photon upconversion, this quenching effect should be even amplified because all of the involved transitions are affected.³⁴ Moreover, subtle changes on the surface-related effects at the nanoscale may induce drastic changes on the luminescence of the NPs, being potentiated as temperature rises, resulting, thus, in an intricate emission temperature dependence.³⁵ Understanding the temperature-dependent luminescence quenching mechanism of UCNPs can not only present an in-depth comprehension of the structure-property relationship at the nanoscale, but also benefit the development of novel nanophotonic materials with particular and intriguing features. In this Perspective, we will firstly review the relevant experimental findings on thermally enhanced UCL in NPs, emphasising the current understandings and the existing puzzles. Lastly, we will provide our viewpoints on this stimulating phenomenon.

Historical perspective on thermally enhanced UCL

Before getting into the review and discussion, a brief summary of the main observations and corresponding interpretations on the thermally enhanced UCL phenomena by distinct research groups in recent years is tabulated in Table 1, which facilitates readers for comparison.

Thermally enhanced UCL was reported back in 2005. Suyver *et al.* reported that the integrated photon flux of Er³⁺ emissions arising from the ⁴I_{13/2}, ⁴S_{3/2}, and ²H_{9/2} excited states in Yb³⁺/Er³⁺ co-doped β-NaYF₄ powder showed a step increase as temperature increased from 10 to 100 K, keeping almost constant when temperature further increased to 200 K.³⁶ Based on high-resolution excitation spectra (Fig. 1a-b) and Yb³⁺ and Er³⁺ energy level structures, the authors explained these observations by a preferable population of the slightly high energy ²F_{5/2}|1> multiplet of Yb³⁺ at high temperatures, which is more energy-resonant with the Er³⁺ ⁴I_{11/2} state, thus resulting in a more efficient Yb³⁺-Er³⁺ ET (Fig. 1c). Later in 2013, Yu *et al.* observed an anomalous luminescence enhancement in Yb³⁺/Er³⁺ co-doped β-NaYF₄ UCNPs with sizes of around 25 and 45 nm and its bulk form in 10-150 K range.³⁷ However, these enhancements only occurred in cryogenic temperatures, whereas the thermal quenching behaviour of UCL was generally reported in a range above RT.³⁸⁻⁴⁰

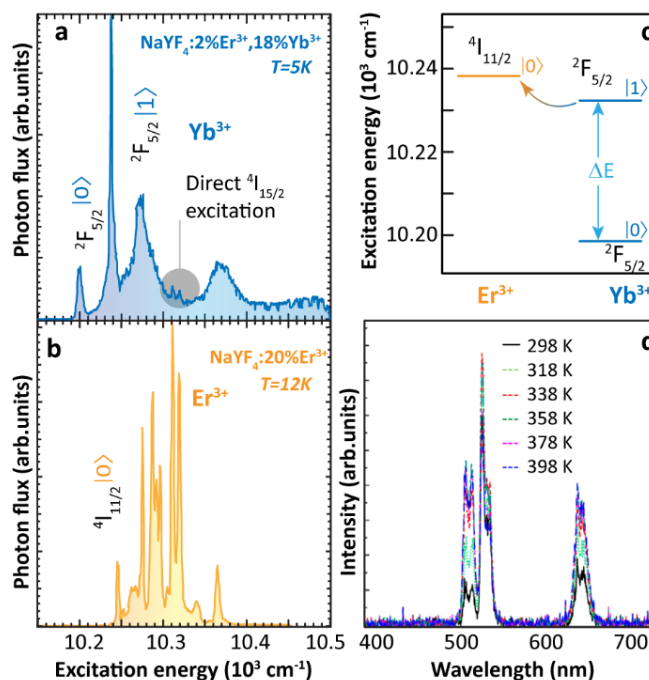


Fig. 1 High-resolution excitation spectra of (a) Yb³⁺/Er³⁺ co-doped and (b) Er³⁺ single-doped β-NaYF₄ bulk samples at low temperatures by monitoring Er³⁺ ⁴S_{3/2}→⁴I_{15/2} transition at 550 nm. (c) Schematic energy level diagram of Yb³⁺ ²F_{5/2} and Er³⁺ ⁴I_{11/2} excited multiplets. Adapted from ref. ³⁶ with permission from Elsevier. (d) Temperature-dependent UCL spectra of 24 nm Yb³⁺/Er³⁺ co-doped β-NaYF₄ UCNPs. Adapted with permission from ref. ²⁹. Copyright (2014) American Chemical Society.

In 2014, Shao's group reported the above-RT thermally enhanced UCL in small-sized Yb³⁺/Er³⁺ co-doped β-NaYF₄ NPs for the first time.²⁹ Upon 975 nm excitation, the UCL intensity of Er³⁺ in the 24 nm-sized UCNPs increased with temperature from 298 to 358 K (Fig. 1d). Preliminary attempts to explore the origin of this result excluded a possible laser-induced recrystallization effect⁴¹ because the observed phenomenon was completely reversible. Also, the increase in excitation light absorptivity was ruled out because no variation was detected in the diffuse reflection spectra of the sample at elevated temperatures. Emission spectra of Er³⁺ under 378 nm direct excitation were recorded at different temperatures and the general luminescence thermal quenching was observed, which foreboded that the sensitizer Yb³⁺ ions played a crucial role in triggering the thermally enhanced UCL. To evaluate the contribution of surface-related effects on the enhancement, the temperature-dependent UCL of core-only and inert-shell coating samples with similar diameters were recorded. The UCL enhancement tendency was observed in both cases. Therefore, the authors claimed no direct relationship between thermally enhanced UCL and surface-related processes. Based on their observations and integrating them with the interpretation of Suyver *et al.*³⁶ and others,⁴² the authors concluded that the thermally enhanced UCL was caused by overcoming the restricted phonon bottleneck effect at high temperatures. Because of the small energy differences (40-90 cm⁻¹) between Yb³⁺ ²F_{7/2}→²F_{5/2} and Er³⁺ ⁴I_{15/2}→⁴I_{11/2} and ⁴I_{11/2}→⁴F_{7/2} transitions, Yb³⁺-Er³⁺ ET process was considered to be active

only with the participation of low-energy phonons. As the particle size was reduced to the nanoscale, the phonon density of states of the material became discrete, and thus these low-energy acoustic phonon modes were cutoff.⁴³ As temperature increased, this phonon confinement effect was weakened, leading to more efficient Yb^{3+} - Er^{3+} ET. In addition, the authors noticed that the luminescence enhancement became more significant with the decrease of the particle size. For instance, the UCL intensity increased about 3 times as temperature increased from 298 to 338 K for 7 nm β - NaGdF_4 nanospheres, while a luminescence thermal quenching was observed when the particle size was larger than 32 nm.²⁹

Deeper understandings of the thermal enhancement mechanism

In 2015, Shao's group observed the thermally enhanced UCL in UCNP with distinct upconversion couples (Yb^{3+} - Ho^{3+} and Yb^{3+} - Tm^{3+})⁴⁴ (Fig. 2a-b). Upon 975 nm excitation, the UCL intensities of large-sized $\text{Yb}^{3+}/\text{Ho}^{3+}$ (or $\text{Yb}^{3+}/\text{Tm}^{3+}$) co-doped β - NaYF_4 nanowires quenched as temperature increased. In contrast, a significant UCL enhancement was observed in all small-sized β - NaGdF_4 UCNP (~ 8 nm), and a weaker enhancement was reported for larger UCNP. Besides, it was observed that the UCL enhancement depended on the activator ion: 52.1 times for Yb^{3+} - Ho^{3+} , 6.2 times for Yb^{3+} - Tm^{3+} , and 3.3 times for Yb^{3+} - Er^{3+} , increasing the temperature from 298 to 398 K. This was tentatively attributed to the different energy matching degrees between the 4f-4f transitions of Yb^{3+} and the activators.

In 2016, Tong *et al.* reported an interesting temperature-dependent UCL variation of $\text{Yb}^{3+}/\text{Er}^{3+}$ co-doped α - NaYF_4 NPs with a size of around 75 nm.⁴⁵ As temperature increased, the UCL intensity of Er^{3+} gradually decreased to a minimum at 483 K and then it increased as temperature further increased to 573 K. Upon cooling, the UCL intensity was recovered (as usual), while a similar but rather weaker "decrease-increase" emission intensity variation reappeared in the subsequent heating phase. The authors suggested that this anomaly was induced by the "adsorption-desorption" process of a small amount of H_2O molecules and other organic solvent residuals on the particle surface at different temperatures.

Shao's group revisited thermally enhanced UCL later in 2017.⁴⁶ Upon 975 nm excitation, they observed that the overall UCL intensities of ultra-small $\text{Yb}^{3+}/\text{Ho}^{3+}$ (or $\text{Yb}^{3+}/\text{Tm}^{3+}$) co-doped β - NaGdF_4 UCNP (< 10 nm) increased as temperature increased from 298 to 423 K. The luminescence spectra of Yb^{3+} in the co-doped sample was then recorded at elevated temperatures, (Fig. 2c) and the luminescence enhancement was detected. Recording the temperature-dependent luminescence decay of the $\text{Yb}^{3+} {}^2\text{F}_{5/2}$ state, all the curves followed a mono-exponential trend and the decay times of $\text{Yb}^{3+} {}^2\text{F}_{5/2}$ state increased on heating (Fig. 2d), pointing out a gradual weakening of the de-excitation of the $\text{Yb}^{3+} {}^2\text{F}_{5/2}$ state. The temperature-dependent UCL intensities of Tm^{3+} were recorded in the core-shell $\text{Yb}^{3+}/\text{Tm}^{3+}$ co-doped UCNP with 3.5 nm thick inert-shell and no UCL enhancement was observed, which was in contradiction

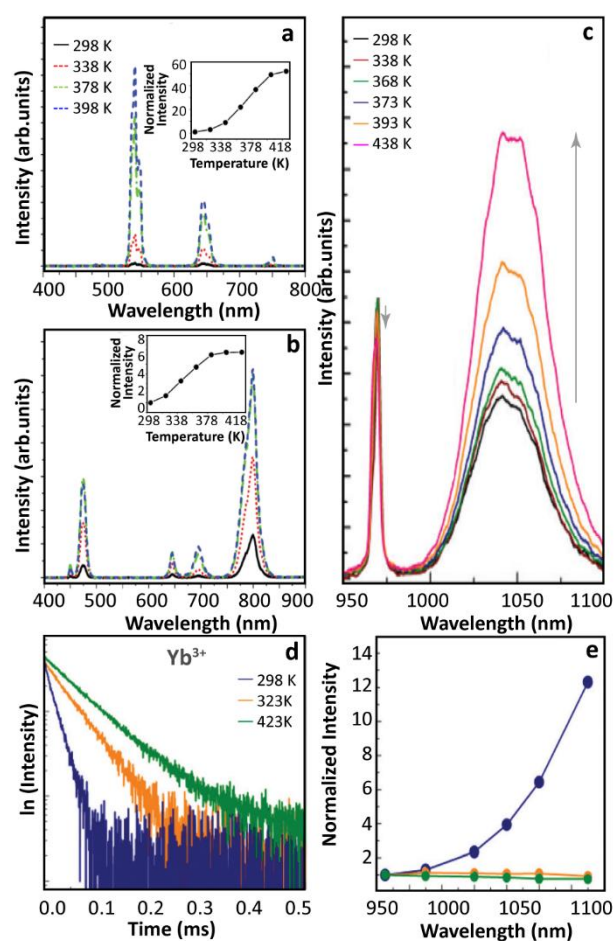


Fig. 2 Temperature-dependent UCL spectra of (a) $\text{Yb}^{3+}/\text{Ho}^{3+}$ and (b) $\text{Yb}^{3+}/\text{Tm}^{3+}$ co-doped β - NaGdF_4 UCNP and the corresponding temperature-dependent integrated intensities. Adapted from ref. ⁴⁴ with permission from the Wiley-VCH. (c) Emission spectra of $\text{Yb}^{3+}/\text{Ho}^{3+}$ co-doped β - NaGdF_4 UCNP with 970 nm excitation and (d) ${}^2\text{F}_{5/2}$ decay curves ($\lambda_{\text{ex}} = 980$ nm, $\lambda_{\text{em}} = 1050$ nm) at different temperatures. (e) Temperature-dependent normalized UCL intensities of core-only $\text{Yb}^{3+}/\text{Tm}^{3+}$ co-doped β - NaGdF_4 UCNP in air (blue), in Ar (green), and $\text{Yb}^{3+}/\text{Tm}^{3+}$ co-doped β - NaGdF_4 @ β - NaGdF_4 core-shell UCNP in air (orange). Adapted from ref. ⁴⁶ with permission from The Royal Society of Chemistry.

with their previous result on the 2 nm thick shell-coating $\text{Yb}^{3+}/\text{Er}^{3+}$ sample.²⁹ Besides, they measured the UCL intensity of core-only $\text{Yb}^{3+}/\text{Tm}^{3+}$ sample in argon (Ar) atmosphere at elevated temperatures which was pre-heated in Ar at 423 K, and a weak thermal quenching was observed (Fig. 2e). Besides, the temperature-dependent emission spectra of this sample were collected dispersing the NPs in 1-octadecene, and the Tm^{3+} UCL intensity decreased monotonously as solution temperature increased. Based on these results, and inspired by the analysis of other researchers,⁴⁷ the authors suggested that the suppression of OH vibration-induced de-excitation of $\text{Yb}^{3+} {}^2\text{F}_{5/2}$ state at high temperatures was the main factor inducing the thermally enhanced UCL, instead of the phonon confinement effect as proposed before.²⁹ According to this rationale, the OH vibrations of H_2O molecules around NPs could induce the luminescence quenching of Yb^{3+} ions situated nearby the particle surface with a certain probability, even when the surface was fulfilled by oleic acid (OA) ligands. A feeble de-excitation of $\text{Yb}^{3+} {}^2\text{F}_{5/2}$ state would cause a severe reduction in the subsequent

excited state population of activator, resulting in a significant UCL quenching in the system. As temperature increased, these H₂O molecules gradually desorbed from the surface weakening the de-excitation of Yb³⁺ ²F_{5/2} state and resulting in the UCL enhancement of the material. Moreover, when temperature decreased some air moisture was again adsorbed on the particle surface and, thus, reversibility was achieved in cycling experiments.

Recent advances and the role of surface for the thermal enhancement of upconversion luminescence

In 2018, Zhou *et al.* provided a new explanation about the thermally enhanced UCL in UCNPs.²⁸ They suggested that an efficient sensitizer-to-activator ET was achieved with the participation of surface phonons generated by the chelating between the Yb³⁺ ions and oxygen atoms on the surface of UCNPs. As temperature increased, more surface phonons were created by the [Yb...O] complexes and immediately coupled with Yb³⁺, then transferred the trapped energy to the Tm³⁺ excited state producing brighter UCL (Fig. 3a). Combining theoretical calculation and Raman spectra, the vibration energies of these surface phonons were estimated to be in the 510–560 cm⁻¹ range. Significant enhancement of Tm³⁺ ¹G₄ luminescence was detected in the core-only Yb³⁺/Tm³⁺ UCNPs with high Yb³⁺ concentration. The UCL intensities of Yb³⁺/Ho³⁺ and Yb³⁺/Er³⁺ samples were recorded at elevated temperatures, and the largest enhancement was detected in Yb³⁺/Tm³⁺ system (Fig. 3b), in clear contradiction with the observations of Shao's group.⁴⁴ In this work, Zhou *et al.* claimed that the contribution of the phonon confinement effect²⁹ on the thermally enhanced UCL was excluded because the enhancement could be also detected in NPs larger than 40 nm (in diameter). Recently, the role of the phonon confinement effect in controlling the relaxation between close-spaced Ln³⁺ Stark levels in ultra-small UCNPs was revisited.⁴⁸ The UCL intensities of Tm³⁺ were also recorded at elevated temperatures in core-shell Yb³⁺/Tm³⁺ co-doped NPs, co-doped NPs after annealing at 773 K and co-doped μm-sized rods. As temperature increased, the thermal quenching of UCL was observed in all the samples, which foreboded that surface phonon was only created by direct chelating between Yb³⁺ and O²⁻ of the surface ligand. Moreover, the authors reported that a decrease in the size of NPs resulted in a more pronounced UCL enhancement, and a 30-fold enhancement of Tm³⁺ luminescence was achieved in the 29 nm-sized co-doped sample. Following this strategy, a record value of a 2000-fold increase in Tm³⁺ ¹G₄ UCL intensity was registered in the 9.7 nm-sized Yb³⁺/Tm³⁺ co-doped UCNPs at 453 K (Fig. 3c). In a consequent work, Liang *et al.* pointed out that this surface phonon essentially resulted in the level-broadening of Yb³⁺ ²F_{5/2} state that reduced the energy mismatch between the 4f-4f transitions of the Yb³⁺ ions and the activators⁴⁹ (Fig. 3d).

In the same year, Lei *et al.* noticed a reversible thermal enhancement of UCL in the 20 nm-sized Yb³⁺/Ln³⁺ (Ln³⁺ = Tm³⁺, Ho³⁺, Er³⁺) co-doped Na₃ZrF₇ UCNPs⁵⁰ (Fig. 3e). This enhancement was detected both in the ligand-free sample and in a sample coated with an inert-shell. It was also observed that

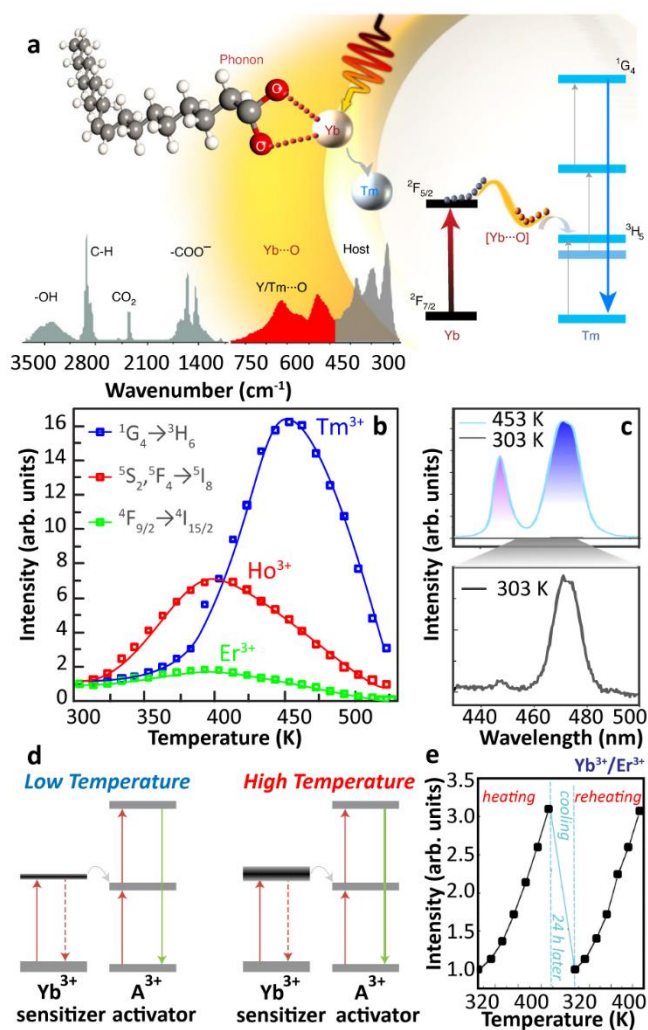


Fig. 3 (a) Schematic illustration of the surface phonon-assisted enhancement mechanism, (b) temperature-dependent normalized UCL intensities of Tm³⁺: ¹G₄→³H₆, Ho³⁺: ⁵S₂(⁵F₄)→⁵I₈ and Er³⁺: ⁴F_{9/2}→⁴I_{15/2} emissions in Yb³⁺/Ln³⁺ (Ln³⁺ = Tm³⁺, Ho³⁺, Er³⁺) co-doped β-NaYF₄ UCNPs with 980 nm excitation, and (c) Tm³⁺ blue emission spectra of 9.7 nm sized Yb³⁺/Tm³⁺ co-doped β-NaYF₄ UCNPs at 453 and 303 K upon 980 nm excitation. Adapted from ref. ²⁸ with permission from the Nature Publishing Group. (d) Level-broadening of Yb³⁺ ²F_{5/2} state at high temperature. Adapted from ref. ⁴⁹ with permission from the Nature Publishing Group. (e) Temperature-dependent normalized UCL intensities of Yb³⁺/Er³⁺ co-doped Na₃ZrF₇ UCNPs upon 980 nm excitation in the heating and reheating phases. Adapted from ref. ⁵⁰ with permission from The Royal Society of Chemistry.

the luminescence enhancement was sensitive to the doping concentration, being a weak thermal quenching detected in the core-only 5%Yb³⁺/20%Lu³⁺/2%Er³⁺ sample. The initial thermally enhanced UCL was recovered after a 15%Yb³⁺-doped active-shell coating. The temperature-dependent UCL intensities of core-only 20%Yb³⁺/2%Er³⁺ UCNPs were measured under different pumping powers, and the enhancement was much larger under high than under low-power excitation. Moreover, the UCL intensity of the sample recorded in a cryogenic temperature range (20–290 K) presented a thermal quenching. Based on first-principles calculations, the authors rationalized their experimental results and stated that the thermal-induced trapped electron release was the dominant process inducing the thermally enhanced UCL. A similar mechanism of trapped

electron releasing was adopted to elucidate the anomalous luminescence enhancement in some bulk optical materials.^{51, 52} Also in 2018, Shao's group raised some questions on the surface phonon-assisted enhancement mechanism²⁸ and presented new evidence supporting their previous understandings on this topic.⁵³ Three distinct Yb³⁺/Ln³⁺ (Ln³⁺ = Tm³⁺, Ho³⁺, Er³⁺) co-doped UCNPs with different diameters, and one co-doped micron-sized rod-like sample were studied. (Fig. 4a) The Ho³⁺-activated UCNPs showed the most significant thermal enhancement of UCL, in accord with their previous results.⁴⁴ Besides, the work presented an intriguing increase in both the luminescence intensities and the ²F_{5/2} decay times with increasing temperature. According to the surface phonon-assisted enhancement mechanism, the UCL enhancement of the activator was achieved at the expense of emission loss of Yb³⁺ because the assistance of surface phonon facilitated the Yb³⁺-to-activator ET causing the decrease of the Yb³⁺ ²F_{5/2} luminescence and the increase of its decay rate, in disagreement with the current results, as pointed out by the authors. The UCL intensities of Yb³⁺/Ln³⁺ co-doped UCNPs were recorded at elevated temperatures in different atmospheres, (Fig. 4b) and the thermally enhanced UCL was found to be closely correlated to the suppression of H₂O molecule-induced quenching effect at high temperatures (Fig. 4c). In the same work, the authors stated that the surface phonon-assisted enhancement mechanism also failed to explain the luminescence thermal quenching behaviour of OA ligand-stabilized Yb³⁺/Ln³⁺ co-doped UCNPs as observed in dry Ar while the surface phonon was certainly formed due to the interaction between the OA ligand and the Yb³⁺ ions.

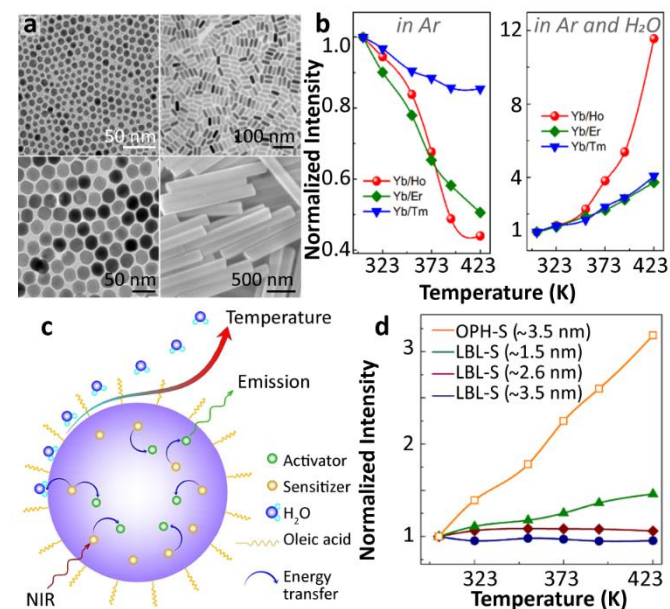


Fig. 4 (a) Morphologies of Yb³⁺/Ln³⁺ co-doped UCNPs, (b) the normalized UCL intensities of Yb³⁺/Ln³⁺ co-doped UCNPs at different temperatures in Ar and Ar/H₂O atmospheres, (c) schematic diagram of thermally enhanced UCL in core-only UCNPs, and (d) temperature-dependent normalized UCL intensities of Yb³⁺/Tm³⁺ co-doped β-NaGdF₄@β-NaGdF₄ core-shell UCNPs with different shell thicknesses synthesized via different shell coating methods. Adapted with permission from ref. ⁵³. Copyright (2018) American Chemical Society.

The authors also noticed that the thermally enhanced UCL was sensitive to other factors, and the effect of shell coating was especially emphasized. In line with their previous report,⁴⁶ the inert-shell as formed by the successive layer-by-layer (LBL) shell-growth method, strongly suppressed the impact of surface moisture on the core luminescence, and the so-called “critical thickness” of inert-shell was estimated to be 3.5 nm (Fig. 4d). This “critical thickness” refers to the shell thickness value for which the UCL enhancement caused by the decoupling of surface OH to the core compensates exactly the intrinsic quenching of core luminescence at elevated temperatures for a given core-shell UCNP, resulting in a temperature-independent UCL. Besides, they found that the thermally enhanced UCL was regenerated in the LBL method shell coating UCNPs if 20%Yb³⁺ were introduced into the shell (active-shell), which implied that the excitation energy of core Yb³⁺ could be delivered through Yb³⁺-to-Yb³⁺ energy migration to the particle surface and quenched by OH vibration of moisture. Intriguingly, different conclusions were drawn by employing an alternative shell coating method (Fig. 4d). Adopting the one-pot heating-up (OPH) shell-growth method, the significant thermally enhanced UCL was detected in the core-(inert)shell NPs, even for shell thickness reaching to 3.5 nm, suggesting an incomplete shielding of the core from the surface moisture.

Understanding the possible underpinning mechanisms explaining the thermal enhancement

Additional efforts were made to unravel the origin of this phenomenon. Lei *et al.* found that the UCL enhancement could be further strengthened exploiting the defects as excitation energy reservoirs through the inequivalence substitution.⁵⁴ In 2019, Martínez *et al.* reported the thermally enhanced UCL in Yb³⁺/Tm³⁺ (or Yb³⁺/Er³⁺) co-doped UCNPs with 2 nm inert-shell coating⁵⁵ (Fig. 5a-b). By doping 20%Yb³⁺ into the shell, a slightly larger UCL enhancement was observed. These works suggested that the luminescence enhancement was associated with the incomplete core shielding by a thin shell and Yb³⁺-to-Yb³⁺ energy migration in the system. Meanwhile, Qiu's group reported the thermally enhanced UCL in core-only Yb³⁺/Tm³⁺ β-NaGdF₄ UCNPs. It was found that the particle sintering process proceeded at high temperatures (>500 K) and caused the irreversible thermal enhancement of UCL⁵⁶ (Fig. 5c-d). Later, Meijerink's group reported the thermally enhanced UCL in a non-fluoride host, Yb³⁺/Ln³⁺ (Ln³⁺ = Tm³⁺, Ho³⁺, Er³⁺) co-doped NaY(WO₄)₂.²⁷ As temperature increased from 300 to 600 K in air, the UCL intensities of activators increased gradually up to the maxima, and then decreased in all of these co-doped UCNPs with different Yb³⁺ concentrations. The decay dynamics of the Er³⁺ ⁴S_{3/2} and ⁴F_{9/2} states were recorded at elevated temperatures in the co-doped sample, and the luminescence rise and decay times became longer as temperature increased, indicating the weakening of nonradiative relaxations in the intermediate and emitting states of Yb³⁺ and Er³⁺. Similar results were obtained for the Er³⁺ single-doped sample. The results of *in situ* temperature-dependent XRD and TEM measurements (Fig. 5e) pointed out that the thermally enhanced UCL was not caused by the thermal-induced phase transition nor by particle

coalescence. The temperature-dependent UCL measurement of co-doped UCNPs was also conducted in dry N_2 , that presented a UCL intensity with reversible thermal quenching/recovering performances in the heating-cooling processes after the first heating-cooling cycle (Fig. 5f). Additionally, the $^2F_{5/2}$ decays in 49% Yb^{3+} doped NPs were measured at elevated temperatures, both in air and dry N_2 . With the increase of the temperature, the $^2F_{5/2}$ decay rate slightly increased in N_2 and significantly decreased in air. Based on these results, the authors proposed that the strong thermally enhanced UCL was ascribed to the removal of surface moisture as temperature increased. To further confirm this hypothesis, thermogravimetric analysis (TGA) and Fourier Transform infrared (FT-IR) measurements were carried out. After the mass loss in the initial TGA heating process, a tiny mass gain (0.5%) of NPs was detected in the cooling phase when temperature was below 370 K (Fig. 5g), which was attributed to the moisture re-adsorption. Moreover, the characteristic OH stretching vibration band was clearly observed in the FT-IR spectrum of sample even after heating treatment at 570 K.

In the same year, Shao's group gave an additional contribution to this discussion investigating the UCNPs luminescence loss mechanisms.⁵⁷ A series of core-shell Yb^{3+}/Er^{3+} doped β -NaGdF₄ NPs with an identical core diameter (5.7 nm) and different shell thicknesses (from 1.1 to 17.7 nm) were studied. The thinnest shell coating co-doped UCNPs were used to record the UCL intensity at elevated temperatures in several atmospheres (air, Ar, Ar/H₂O, and Ar/D₂O). The thermal enhancement of UCL was observed in the H₂O containing atmospheres, and the thermal quenching was observed in the other atmospheres, ratifying the importance of the moisture-induced effect. Distinctly from what they reported before, the authors argued that the direct coupling of Yb^{3+} $^2F_{5/2}$ excited state to the OH overtone vibration of the H₂O molecule (instead of the OH fundamental vibration-involved multiphonon relaxation), was the main pathway inducing the strong de-excitation of the $^2F_{5/2}$ state, leading to significant UCL quenching. This was supported by the comparison between the emission spectrum of Yb^{3+} and the absorption spectrum of H₂O (Fig. 5h). Additionally, the temperature dependence of UCL intensities was recorded for these samples. A "critical thickness" of 5.4 nm was obtained, a value 1.5 times larger than that reported before.⁵³ The $^2F_{5/2}$ luminescence decay in these samples permitted the authors to conclude that the maximum coupling distance of excited Yb^{3+} and the OH vibration of surface H₂O was of the order of 11 nm.

Thermal enhancement in NPs with distinct upconversion mechanisms

Despite the observation of thermally enhanced UCL in the systems displaying "ET upconversion" couples, some researchers found the similar phenomenon in other types of upconversion pairs, as complying with "cooperative upconversion" mechanisms, such as Yb^{3+} - Tb^{3+} and Yb^{3+} - Eu^{3+} . In 2017, Chen's group reported the multiphoton UCL of the Tb^{3+} 5D_3 and 5D_4 states in Tb^{3+} -doped $LiYbF_4$ NPs upon high-density

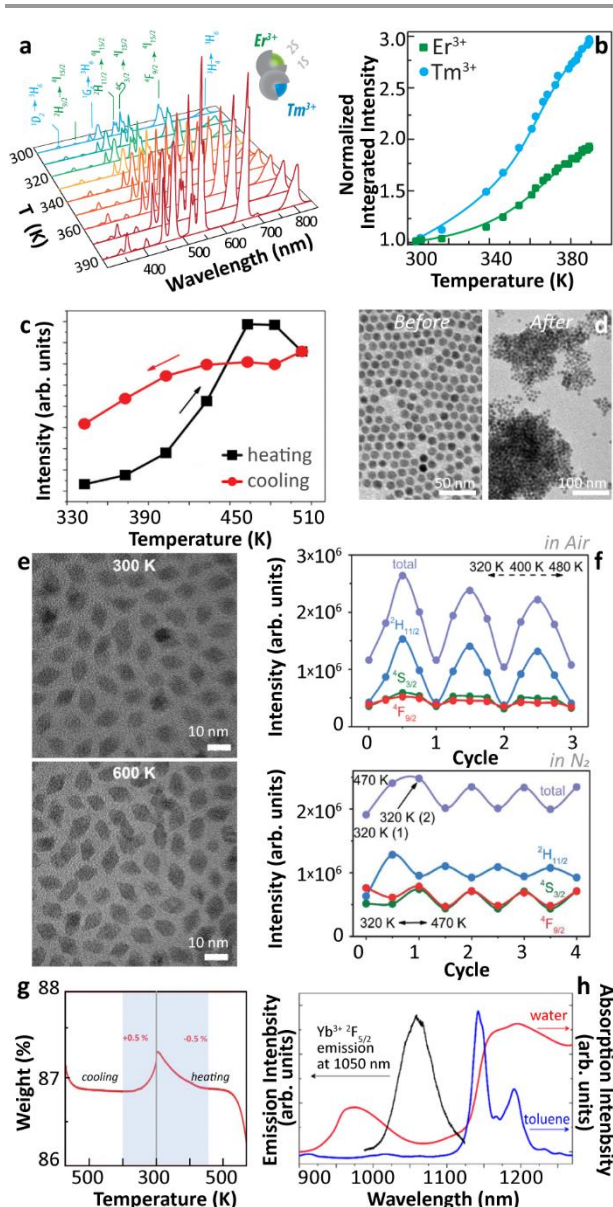


Fig. 5 (a) Temperature-dependent UCL spectra upon 980 nm excitation of the heterogeneous system containing two different kinds of Yb^{3+}/Ln^{3+} ($Ln^{3+} = Er^{3+}, Tm$) co-doped β -NaGdF₄ UCNPs deposited onto a AgNWs/PMMA film and (b) the corresponding integrated intensities of overall Er^{3+} (or Tm^{3+}) 4f-4f emissions in the whole spectra at different temperatures. Adapted from ref. ⁵⁵ with permission from the Wiley-VCH. (c) $Tm^{3+} \ ^1G_4 \rightarrow \ ^3H_6$ UCL intensities of Yb^{3+}/Tm^{3+} co-doped β -NaGdF₄ UCNPs in one "heating-cooling" cycle and (d) the corresponding sample morphology changes before and after heating to 565 K. Adapted from ref. ⁵⁶ with permission from The Royal Society of Chemistry. (e) Morphology of Yb^{3+}/Er^{3+} co-doped $NaY(WO_4)_2$ UCNPs at 300 and 600 K, (f) temperature-dependent UCL intensities of Yb^{3+}/Er^{3+} co-doped NPs within a continuous "heating-cooling" cycle in air or N_2 upon 980 nm excitation, and (g) TGA of the sample in first cooling and reheating phases in air. Adapted from ref. ²⁷ with permission from The Royal Society of Chemistry. (h) $Yb^{3+} \ ^2F_{5/2}$ emission spectrum of Yb^{3+}/Er^{3+} co-doped β -NaGdF₄@ β -NaGdF₄ core-shell UCNPs and the absorption spectra of H₂O and toluene. Adapted with permission from ref. ⁵⁷. Copyright (2019) American Chemical Society.

980 nm laser excitation.⁵⁸ As temperature increased from 10 to 300 K, the overall UCL intensity increased almost an order of magnitude with the gradual decrease of Yb^{3+} luminescence in 30% Tb^{3+} -doped UCNPs (Fig. 6a-b). The authors attributed their observations to the temperature-induced increasing of the

population of the high-energy Stark level of the $\text{Yb}^{3+} \ ^2\text{F}_{5/2}$ state. This increase favoured the phonon-assisted upconversion process, resulting in a noteworthy UCL enhancement (Fig. 6c). In the same year, Wang's group reported a reversible thermally enhanced UCL in $\text{Yb}^{3+}/\text{Eu}^{3+}$ co-doped $\beta\text{-NaGdF}_4$ UCNPs.⁵⁹ Heating the particles from 300 to 423 K, the UCL of Eu^{3+} showed a 16-fold enhancement in 20% $\text{Yb}^{3+}/10\%\text{Eu}^{3+}$ co-doped $\beta\text{-NaGdF}_4$ upon 980 nm excitation (Fig. 6d). Moreover, this enhancement exhibited a dependence on the particle size, which was more significant for the smaller UCNPs. Noteworthy, the absolute UCL intensity of large-sized NPs was always stronger than that of small-sized NPs (even at high temperatures), and thus the thermally enhanced UCL was associated with the surface-related effects. The Yb^{3+} -to- Yb^{3+} energy migration was regarded as the main non-radiative deactivation pathway⁶⁰ which was further supported by the observation of a gradual decrease of the $^2\text{F}_{5/2}$ decay rate in the co-doped sample as temperature increased. Additionally, a slight thermal-induced lattice expansion was detected. Besides that, the UCL intensity of Eu^{3+} in the core-shell co-doped UCNPs was recorded at elevated temperatures, and a weak luminescence enhancement was also discerned. Based on these

observations, a different enhancement mechanism was suggested (Fig. 6e). As temperature increased, the averaged Yb^{3+} - Yb^{3+} distance becomes larger due to the lattice expansion, leading to a deactivation of Yb^{3+} -to- Yb^{3+} energy migration, therefore, suppressing the surface-related quenching effect. Consequently, the Yb^{3+} -to-activators ET was favoured which resulted in the thermally enhanced UCL.

Emerging applications for thermally enhanced UCNPs

Apart from the basic comprehension of the thermally enhanced UCL, it soon becomes clear that this phenomenon can be definitively used for conceiving innovative solutions in luminescence thermometry, thermochromism, and lithography.

Luminescence thermometry

Luminescence thermometry is a technique using the thermal dependence of the photophysical properties of a given material to determine the temperature of its surroundings. One of the most interesting classes of phosphors for luminescence thermometry is Ln^{3+} -doped materials. The applications of Ln^{3+} ions in luminescence thermometry was recently reviewed by some of us,^{61, 62} however, several other reviews not circumscribed to Ln^{3+} ions were also published.⁶³⁻⁶⁵ The ladder-like energy levels of Ln^{3+} ions make them unique probes for thermometry applications. As the separation of the 4f energy levels is on the order of hundreds of cm^{-1} , it can be easily bridged near RT (so-called thermally coupled energy levels) by thermal redistribution, which is governed by the Boltzmann law. For the illustrative example of two thermally coupled emitting levels whose energy difference between the barycentres of the $2 \rightarrow 0$ and $1 \rightarrow 0$ emission bands is ΔE , the $2 \rightarrow 0$ (I_2) and $1 \rightarrow 0$ (I_1) intensity ratio is given by:

$$\frac{I_2}{I_1} = \frac{\hbar\omega_{02}A_{02}N_2}{\hbar\omega_{01}A_{01}N_1} = \frac{\omega_{02}A_{02}g_2}{\omega_{01}A_{01}g_1} \exp\left(-\frac{\Delta E}{k_B T}\right) = B \exp\left(-\frac{\Delta E}{k_B T}\right) \quad (1)$$

where A_{01} and A_{02} and ω_{01} and ω_{02} are, respectively, the total spontaneous emission rates and the angular frequencies of the $1 \rightarrow 0$ and $2 \rightarrow 0$ transitions, N_1 and N_2 the populations of states $|1\rangle$ and $|2\rangle$, g_1 and g_2 are the degeneracies of the 1 and 2 levels, k_B is the Boltzmann constant, and T is the absolute temperature. The UCNPs-based thermometers exploit the intensity ratio of two emissions originated from thermally coupled energy levels and are intrinsically primary thermometers (*i.e.* the temperature can be calculated avoiding any calibration process). In contrast, the thermometers that are referred to an external temperature reference requiring a calibration procedure are termed as secondary thermometers. The restriction to the energy difference ΔE in the examples involving thermally coupled levels (to ensure the strong coupling, typically $\Delta E < 1000 \text{ cm}^{-1}$) precludes relative thermal sensitivities (S_r) values near RT higher than $1.5\% \text{ K}^{-1}$.⁶⁶ Larger ΔE between

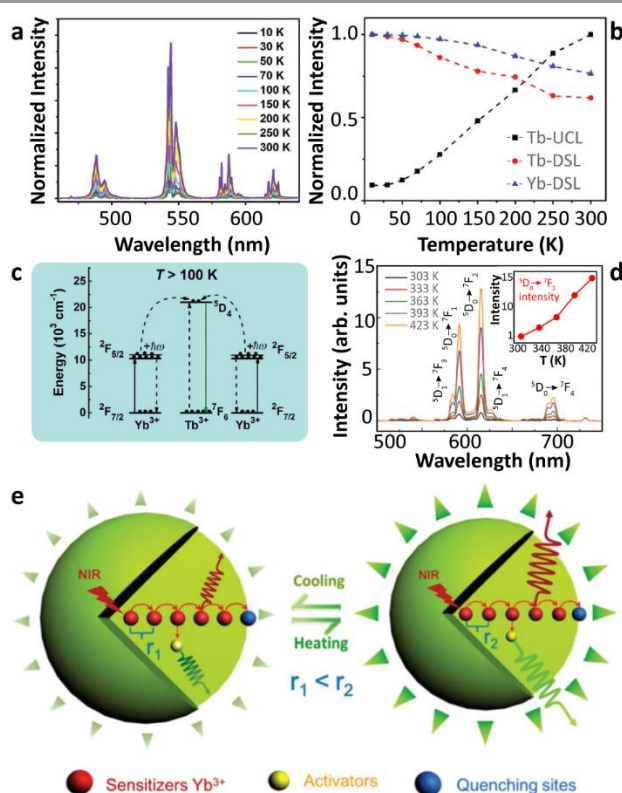


Fig. 6 (a) Temperature-dependent UCL spectra of $\text{LiYbF}_4:30\%\text{Tb}^{3+}/\text{LiYF}_4$ core-shell UCNPs upon 980 nm excitation and (b) the corresponding temperature-dependent normalized Tb^{3+} and Yb^{3+} emission intensities, and (c) the schematic illustration of phonon-assisted “cooperative upconversion” mechanism. Adapted from ref.⁵⁸ with permission from The Royal Society of Chemistry. (d) Temperature-dependent UCL spectra of $\text{Yb}^{3+}/\text{Eu}^{3+}$ co-doped $\beta\text{-NaGdF}_4$ UCNPs upon 980 nm excitation and the inset showed the corresponding normalized $\text{Eu}^{3+} \ ^5\text{D}_0 \rightarrow \ ^7\text{F}_2$ emission intensities as a function of temperature, (e) the schematic illustration of lattice thermal expansion-induced quenching suppression mechanism. Adapted from ref.⁵⁹ with permission from The Royal Society of Chemistry.

the thermally coupled levels decreases the thermalization of the upper $|2\rangle$ level, resulting in lower luminescence intensity. To overcome this bottleneck, strategies for designing novel luminescence intensity ratio-based thermometers to further improve S_r should be considered other than the thermally coupled strategy, besides playing with the size of UCNPs or with the phonon energy of the hosts. The wisest approaches consist of using two distinct (and thermally decoupled) emission lines of the same Ln^{3+} ion or two emitting levels of distinct centres. A recent review by Cheng *et al.*⁶⁶ discussed in detail these strategies for improving the thermometric performance based on the “fully-decoupled” or “moderately-coupled” emitting levels or emitting levels in which ET was mediated or thermally assisted by host or ligand energy levels.

The conventional thermal quenching is responsible for narrowing the operating temperature range of the luminescent thermometers because when the intensity of the transitions reaches the baseline fluctuations the device luminescent thermometer falls out of its operating range. Therefore, the thermally enhanced UCL offers the possibility of overcoming this limitation, and thus the strong luminescence at high temperatures is easily recorded even using cost-effective portable detectors. Regarding the thermal dependence of the S_r , the well-known inverse proportionality with temperature squared precludes S_r values beyond $1\% \text{ K}^{-1}$ for temperature above 400 K. However, this rule is relaxed when the value of temperature is derived from the ratio between non-thermally coupled transitions, and higher S_r are achievable.

There are still a few works exploiting the thermally enhanced UCL for producing high-sensitive nanothermometers. Following the pioneering work of Shao's group in 2014,²⁹ the utility of thermally enhanced UCL was harnessed almost immediately. In 2015, Shao's group reported the application of UCNPs with different sizes as a strategy for the development of materials for luminescence thermometry.⁴⁴ They formed dry nanopowders combining large-sized $\text{Yb}^{3+}/\text{Ho}^{3+}$ (or $\text{Yb}^{3+}/\text{Tm}^{3+}$) NaYF_4 nanowires with $\text{Yb}^{3+}/\text{Tm}^{3+}$ (or $\text{Yb}^{3+}/\text{Ho}^{3+}$) NaGdF_4 NPs ($\sim 8 \text{ nm}$). In 2019 Martínez *et al.* used nanocomposite transparent films combining a poly(methyl methacrylate) (PMMA) matrix and a percolating network of silver nanowires (AgNWs) to control the local temperature and therefore to fine-tune the emission intensity of UCNPs⁵⁵ (Fig. 7a-b). The concept was to use nanocomposites formed by two types of UCNPs with opposite luminescence thermal responses, one containing Er^{3+} and the other containing Tm^{3+} ions. As the UCL intensity of the smaller of particles increased with the increase in temperature while that of the larger ones decreased, making the value of S_r considerably higher.

Using the ratio of intensities between the ${}^1\text{G}_4 \rightarrow {}^3\text{H}_6$ (originated in small-sized Tm^{3+} doped NPs) and the ${}^4\text{S}_{3/2} \rightarrow {}^4\text{I}_{15/2}$ (originated in large-sized Er^{3+} doped NPs) a maximum value of S_r ($5.88\% \text{ K}^{-1}$ at 339 K) was reported. This constituted a more than 6-fold improvement relative to the value calculated at the same temperature using the commonly reported ratio between the $\text{Er}^{3+} {}^4\text{S}_{3/2} \rightarrow {}^4\text{I}_{15/2}/{}^2\text{H}_{11/2} \rightarrow {}^4\text{I}_{15/2}$ transitions in the green spectral range. As an added benefit the intensity ratio involving the ${}^4\text{S}_{3/2}$ and ${}^2\text{H}_{11/2}$ levels was found to be independent of the size of NPs,

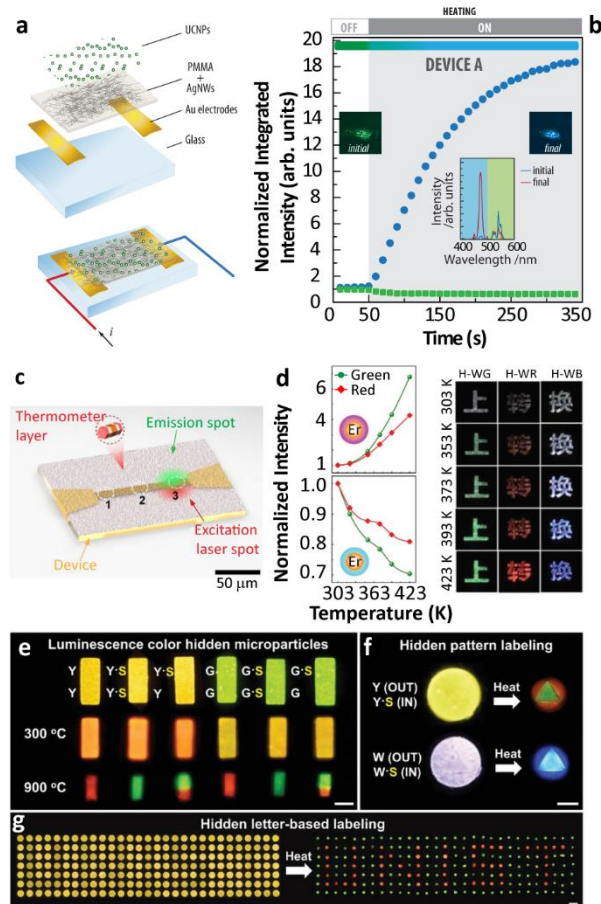


Fig. 7 (a) Exploded view and schematic of an assembled electrothermal device and (b) the UCL intensity and overall luminescence colour change of device upon electrothermal control. Reproduced from ref.⁵⁵ with permission from the Wiley-VCH. (c) The illustration of real-time sensing of local temperature changes on a microelectronic device coated with nanothermometers. Reprinted with permission from ref.⁶⁷. Copyright (2019) American Chemical Society. (d) Temperature-dependent UCL of $\text{Yb}^{3+}/\text{Er}^{3+} \text{NaGdF}_4$ UCNPs with inert-shell or Yb^{3+} -doped active-shell coating, and temperature-responsive colour changes of Chinese characters printed with the corresponding hybrid inks. Reproduced from ref.⁶⁸ with permission from the Wiley-VCH. (e) Temperature-sensitive luminescence colour hidden microparticles, (f) hidden pattern- and (g) hidden letter-based labelling system. Reproduced from ref.⁶⁹ with permission from the Wiley-VCH.

the morphology and phase of host lattice, constituting an inner primary thermometer that was very useful for the system calibration.

In a further development of the same strategy, the same authors extended the concept of reporting how $\text{Yb}^{3+}/\text{Er}^{3+}$ and $\text{Yb}^{3+}/\text{Tm}^{3+}$ co-doped UCNPs of distinct sizes embedding PMMA films could be used to fabricate self-calibrated double luminescent thermometers.⁷⁰ Moreover, this report assessed the figures-of-merit of thermometers by combining mixtures of UCNPs with distinct sizes (e.g., large-sized Er^{3+} - and small-sized Tm^{3+} -doped UCNPs and small-sized Er^{3+} - and large-sized Tm^{3+} -doped UCNPs). As the nanocomposites contained a primary thermometer operating based on the $\text{Er}^{3+} {}^4\text{S}_{3/2} \rightarrow {}^4\text{I}_{15/2}/{}^2\text{H}_{11/2} \rightarrow {}^4\text{I}_{15/2}$ transitions and a secondary thermometer that used the intensity ratio of Tm^{3+} and Er^{3+} transitions, the primary thermometer was used to calibrate the secondary one (that displayed a higher S_r and a lower

temperature uncertainty), avoiding recurrent and time-consuming calibration procedures whenever the system operated in new experimental conditions.

A recent work of Jin's group explored the same strategy to boost the value of S_r in UCNPs.⁶⁷ The concept of opposite thermally affected luminescence behaviour was exploited by constructing heterogeneous Ln³⁺-doped UCNPs for dual-emitting centres-based thermometry. By multistep synthesis, the authors fabricated UCNPs with selected regions co-doped with Yb³⁺/Nd³⁺ or Yb³⁺/Er³⁺ displaying thermally enhanced or quenching performances, respectively. Following this strategy, a record-breaking S_r (9.6% K⁻¹ at RT) was achieved. The nanoparticles were then successfully used to probe the local temperature in an electrical track dissipating energy by Joule effect (Fig. 7c).

Thermochromism

The opposite temperature-dependent UCL features of each set of particles resulted in a thermochromic luminescence of mixed powder, whereby the emission colour shifted from green to blue depending exclusively on temperature. Shao's group applied this concept for the development of anti-counterfeiting technologies.^{46, 71} This idea was then followed by Lei and collaborators who worked on the engineering of crystal defects in UCNPs to improve the thermally enhanced luminescence properties. They confirmed the usefulness of Yb³⁺/Ln³⁺ co-doped Na₃ZrF₇ UCNPs for thermochromic inks.⁵⁰ Soon after, the same authors proposed the addition of low valence dopant ions (mainly Ca²⁺) in the composition of NaGdF₄-based UCNPs to further improve the thermally enhanced UCL and the thermochromic performance of composite inks.⁵⁴

Through rational design and controlled synthesis, Hu *et al.* recently presented thermochromic nanocomposite inks based in the combination of small-sized UCNPs with inert-shell or Yb³⁺-doped active-shell coatings.⁶⁸ Because of different thermally induced luminescence variation tendencies of adopted shell coating UCNPs, the emission colour of nanocomposite inks could shift throughout the chromaticity diagram following the increase in temperature. (Fig. 7d) Recent works also showed that the thermochromic performance was obtained in other systems by employing the thermally enhanced UCL behaviour of materials. Zou *et al.* reported a unique thermally induced lattice contraction in Er³⁺-doped Yb₂W₃O₁₂ bulk material.⁷² As temperature increased from 303 to 573 K, a more efficient Yb³⁺-Er³⁺ ET occurred in the system, which resulted in a 29-fold enhancement of green upconversion emission. Continuing this work, they found a 5-fold UCL enhancement in the analogous Yb³⁺/Ho³⁺ co-doped Sc₂Mo₃O₁₂ as temperature rose, and a significant luminescence colour shift was achieved accordingly.⁷³

A step forward in thermochromic nanocomposites is the integration of UCNPs with heating elements that can control electrically the local temperature around luminescence emitters. With this idea, Martínez *et al.* developed bilayer systems formed by a semi-transparent conductive bottom layer and a top layer formed by UCNPs.⁵⁵ (Fig. 7a) The temperature increase was controlled by the bottom layer and resulted in the

luminescence enhancement or quenching of small-sized or large-sized UCNPs, respectively, which allowed to control electrically the emission colour throughout the chromatic scale. An important feature was that the structure could be formed on flexible and transparent substrates opening the door for optoelectronic flexible devices.²⁵

Lithography

The ability to include UCNPs in optical and optoelectronic devices in a localized and selective manner is one of the objectives sought. In this regard, several authors have shown the possibility of applying different lithography techniques to pattern UCNPs.⁷⁴⁻⁷⁶ Although most works did not harvest the phenomenon of thermally enhanced UCL, recent developments have taken this feature into account. Baek and co-workers developed a maskless flow lithography technique dispersing Ln³⁺-doped NaYF₄ UCNPs and SiO₂ NPs in a photocurable resin (polyurethane acrylate).⁶⁹ (Fig. 7e-g) The polymer solution was flown into a polydimethylsiloxane (PDMS) microfluidic channel and polymerized with patterned UV light. The subsequent thermal treatment resulted in the UCL enhancement of material, which demonstrated the application potential in the multiple colour encryption field. Martínez and co-workers developed a maskless lithography method based on the photothermal action of gold nanostars deposited over a thermoplastic nanocomposite containing small-sized UCNPs.⁷⁷ The thermally enhanced UCL in Er³⁺-doped UCNPs was analysed to probe the local temperature in the laser spot used for writing, and luminescence patterns on rigid and flexible substrates were produced.

Discussion

Based on the above extensive revision, we can easily realize that many contradictory experimental findings have been reported and some incompatible explanations have been proposed to address the origin of thermally enhanced UCL. The rapid desorption of surface-attached H₂O molecule at high temperatures is regarded as one of the most likely inducements. It has been reported that the massive luminescence quenching of Ln³⁺-doped UCNPs was observed when dispersing in aqueous solution,⁷⁸⁻⁸⁰ and the OH vibration was regarded as the most deleterious cause. Because of large SVR, NPs exposed to air have a certain probability of adsorbing the moisture in air and forming a hydration layer around the particle surface. Therefore, the luminescence properties of UCNPs even in the powder form will be affected by the H₂O molecule-induced quenching effect. If so, the thermal-induced UCL enhancement can be roughly regarded as a recovery process through which the sample regains the emission features missed due to the quenching effects. In order to deeply comprehend the nature of thermally enhanced UCL in UCNPs, a clear and beforehand understanding about the detailed luminescence quenching mechanism of involved Ln³⁺ in the system is essential. In this section, this issue will be explicitly discussed.

Luminescence properties of optical material are strongly associated with the ambient medium. For Ln³⁺-doped UCNPs, the medium-dominated effect can not only affect the intrinsic radiative transition rate of the centre but also have a great impact on the nonradiative relaxation probabilities of their excited states.⁸¹ The former can be well-described by the local-field effect,^{82, 83} and the latter is largely controlled by multiple processes. One of the dominant processes is the solvent quenching effect by vibration coupling. Provided that UCNPs are dispersed in H₂O, the nonradiative relaxation between two closely spaced states will be triggered with the participation of suitable vibrations of the H₂O molecule, resulting in a noticeable de-excitation of the upper energy state. In 2015, Arppe *et al.* studied the H₂O molecule-induced quenching effect on the luminescence of core-only Yb³⁺/Er³⁺ (or Yb³⁺/Tm³⁺) co-doped NPs.⁴⁷ Upon 380 nm excitation, the luminescence decay of Er³⁺ ⁴S_{3/2} state in the co-doped sample was faster in H₂O than in deuterated water (D₂O, with much lower OD vibrational energy) as shown in Fig. 8a, while the luminescence decay of Er³⁺ ⁴F_{9/2} state was almost identical in these two solutions. Supplemental experiments further revealed that the intensity of the ⁴F_{9/2}→⁴I_{15/2} transition in this sample remained constant as increasing the proportion of H₂O in D₂O (Fig. 8b). These results indicated that the OH vibration contributed differently to the quenching behaviour of Er³⁺ visible luminescence from different excited levels. Besides, it showed that the decay rates of Yb³⁺ ²F_{5/2} luminescence in H₂O were always faster than those in D₂O (Fig. 8c). Consequently, the authors concluded that the direct de-excitation of Yb³⁺ ²F_{5/2} state through the coupling interaction with the OH vibration of H₂O was the main factor causing the UCL quenching in the system. Moreover, the authors suggested that the long-range Yb³⁺-to-Yb³⁺ energy migration would let all Yb³⁺ ions in the particle being strongly susceptible to the quenching effect of OH vibration because of the high concentration of Yb³⁺ in the general-studied UCNPs.⁸⁴ Despite experiments have showed that the presence of H₂O certainly induced the strong luminescence loss of material, few works were published exploring the underlying mechanism behind the phenomena.⁸⁵⁻⁸⁸ A full understanding of this issue requires not only the clear comprehension of the UCL mechanism⁸⁹⁻⁹³ but also the knowledge of the effect of OH vibration on the excited electron population^{86, 94} and subsequent luminescence dynamics of each excited state involved in the upconversion process.⁹⁵ In addition, attention should be paid to consider the synergistic effects imposed by the other variables on the luminescence properties of the material,⁹⁶ such as laser-induced local heating and the delocalization of dopants within the structure. Fortunately, some attempts have been made to reveal the solvent molecule-induced luminescence quenching mechanism of Ln³⁺ and the results are helpful to comprehend the nature of thermally enhanced UCL in Ln³⁺-doped UCNPs.

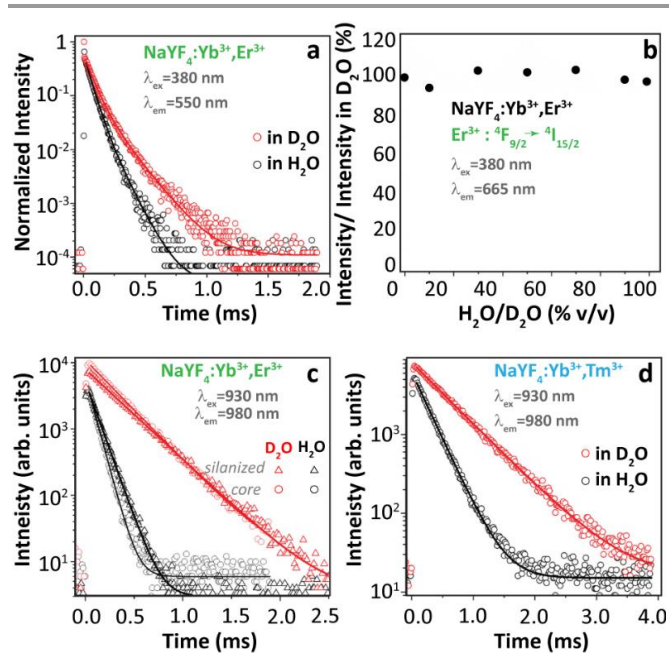


Fig. 8 (a) Decay curves of Er³⁺ ⁴S_{3/2}→⁴I_{15/2} luminescence ($\lambda_{\text{ex}} = 380 \text{ nm}$, $\lambda_{\text{em}} = 550 \text{ nm}$) in Yb³⁺/Er³⁺ co-doped β -NaYF₄ UCNPs in H₂O and in D₂O, (b) normalized emission intensities of Er³⁺ ⁴F_{9/2}→⁴I_{15/2} luminescence upon 380 nm excitation in D₂O with increasing the proportion of H₂O, (c, d) Decay curves of Yb³⁺ ²F_{5/2}→²F_{7/2} luminescence ($\lambda_{\text{ex}} = 930 \text{ nm}$, $\lambda_{\text{em}} = 980 \text{ nm}$) in Yb³⁺/Er³⁺ and Yb³⁺/Tm³⁺ co-doped UCNPs with or without a silica shell in H₂O and in D₂O. Reproduced from ref. ⁴⁷ with permission from The Royal Society of Chemistry.

Solvent-induced quenching

Started in 2018, Meijerink's group has focused their attention on understanding the luminescence quenching mechanism in UCNPs. The main motivation of their works is attempted to give a quantitative interpretation of luminescence quenching behaviour of Ln³⁺ ions. In their first report³⁵, they developed a solvent quenching model on the basis of Förster resonant ET (FRET) mechanism, which could simulate the luminescence decay dynamics of Er³⁺ and Yb³⁺ excited states when the samples were dispersed in different organic solvents (Fig. 9a). The analyses of the solvent quenching effect on luminescence decays of Er³⁺ ⁴S_{3/2} and ⁴F_{9/2} states were initially performed in the core-only and core-shell 0.1% Er³⁺ doped samples (Fig. 9b-g). Considering the small energy gaps (3200 and 2800 cm⁻¹) of ⁴S_{3/2} and ⁴F_{9/2} states to their next-lower-energy states (⁴F_{9/2} and ⁴I_{9/2}, respectively), the nonradiative relaxation induced by the CH stretching vibration of solvent molecules (~3000 cm⁻¹) was significant in core-only samples. Also, it showed that the solvent quenching effect on the luminescence of the ⁴S_{3/2} state was weaker than that of the ⁴F_{9/2} one because of the relatively lower oscillator strength of the ⁴S_{3/2}→⁴F_{9/2} transition than that of ⁴F_{9/2}→⁴I_{9/2}.⁹⁷ Besides, a stronger quenching of Er³⁺ ⁴F_{9/2} luminescence was detected in aliphatic solutions than in aromatic ones (Fig. 9f), and more adaptive energy resonance of the ⁴F_{9/2}→⁴I_{9/2} relaxation and the CH stretching vibration in aliphatic solutions served as the main cause. Experimental results also confirmed the strong suppression of inert-shell coating to the solvent quenching effect in the core-shell NPs. More significant luminescence quenching was observed in the Er³⁺-doped NPs with high doping concentration (2%Er³⁺ and

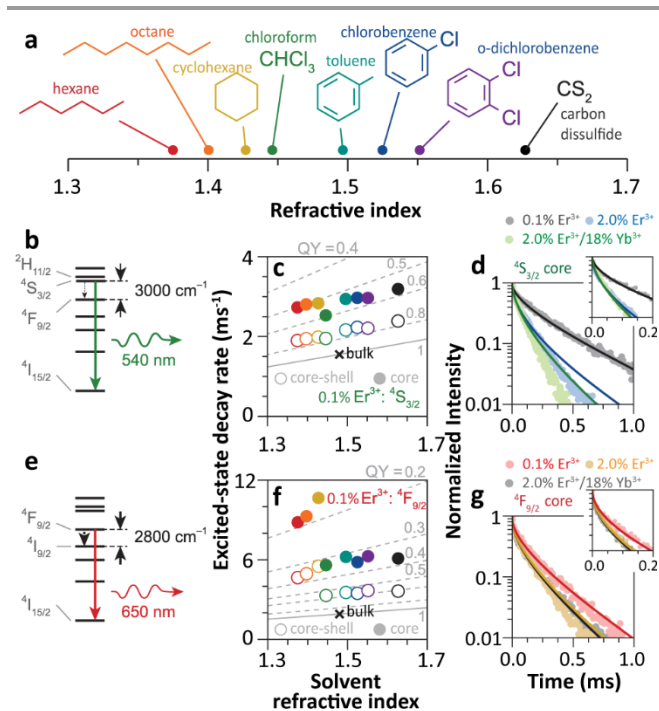


Fig. 9 (a) Refractive index of different organic solvents. Please note the color code that will be used along of the work. (b) Energy diagram of $\text{Er}^{3+} 4S_{3/2}$ state, (c) averaged decay rates of $4S_{3/2}$ state in 0.1% Er^{3+} -doped $\beta\text{-NaYF}_4$ NPs with core-only and core-shell geometries in the different solvents indicated in (a). The dashed lines represent the simulated QY values (estimated as the ratio of radiative decay rate and the total decay rate of a luminescence centre in a nanocrystal). (d) decay curves of $4S_{3/2}$ luminescence in core-only NPs when dispersing in toluene with different concentrations and the corresponding model simulation results, the inset showed a zoom-in in the initial period. (e) Energy diagram of $\text{Er}^{3+} 4F_{9/2}$ state, (f) averaged decay rates of $4F_{9/2}$ state in Er^{3+} -doped $\beta\text{-NaYF}_4$ samples in different solvents, and (g) decay curves of $4F_{9/2}$ luminescence in core-only NPs when dispersing in toluene and the corresponding simulation results. Adapted with permission from ref. ³⁵. Copyright (2018) American Chemical Society.

2% Er^{3+} /18% Yb^{3+}). The solvent-quenching model perfectly described the luminescence decays of $\text{Er}^{3+} 4S_{3/2}$ states in these core-shell NPs. However, the simulation only described the initial parts of the $4S_{3/2}$ decays in the core-only NPs (blue and green curves in Fig. 9d), and the experimental decay became faster than the simulation in the later period. The authors proposed that it was caused by an efficient Er^{3+} -to- Er^{3+} energy migration to the particle surface, being rapidly quenched by toluene molecules. In contrast, the model successfully simulated the decays of $\text{Er}^{3+} 4F_{9/2}$ luminescence in these core-only NPs in toluene (Fig. 9g), and a feeble contribution of energy migration was detected.

The solvent quenching effect on the infrared luminescence of $\text{Er}^{3+} 4I_{11/2}$ and $\text{Yb}^{3+} 2F_{5/2}$ states was also studied (Fig. 10). Almost complete quenching (98%) was detected for $\text{Er}^{3+} 4I_{11/2}$ luminescence in the core-only 2% Er^{3+} single-doped sample in all solvents (Fig. 10b). Considering the small energy gap of the $\text{Er}^{3+} 4I_{11/2} \rightarrow 4I_{13/2}$ transition (3500 cm^{-1}), the solvent quenching effect was expected to be strong. Surprisingly, the luminescence decay of $\text{Er}^{3+} 4I_{11/2}$ state could not be described by the model at all, neither in core-only nor in core-shell NPs (Fig. 10d), and the authors believed that the OH impurity in the crystal structure, introduced during the synthesis, was the main quenching centre, especially in the core-shell samples. In contrast, the

solvent quenching effect on the $\text{Yb}^{3+} 2F_{5/2}$ luminescence was expected to be insignificant considering the large $2F_{5/2} \rightarrow 2F_{7/2}$ energy gap. While in the core-only 18% Yb^{3+} doped sample, a strong luminescence quenching of $\text{Yb}^{3+} 2F_{5/2}$ state was observed, and the undercoordinated Yb^{3+} on the particle surface was regarded as the main quenching centre. Shell passivation effect was very efficient, leading to an increase of almost one order of magnitude of the $2F_{5/2}$ luminescence in the core-shell 18% Yb^{3+} single-doped NPs (Fig. 10c). Moreover, the result showed that the decay of $2F_{5/2}$ luminescence in the co-doped sample was much faster than that in the single-doped one. (Fig. 10e) Later, Huang *et al.* raised some doubts about the explanations provided by Meijerink's group.⁹⁸ They suggested that the main quenching pathway of $\text{Yb}^{3+} 2F_{5/2}$ luminescence was the coupling interaction between the $2F_{5/2} \rightarrow 2F_{7/2}$ transition and the overtone vibration of the solvent molecules in the solution,⁹⁹ instead of the quenching by uncoordinated Yb^{3+} ions. An overtone transition is defined as the transition between two states separated by more than one vibrational quantum.^{100, 101} The oscillator strength of the 1-overtone transitions is typically two orders of magnitude weaker than that of the fundamental transition, and each the successive overtone is roughly one order of magnitude weaker.¹⁰¹ Huang *et al.* claimed that the quenching effect of the OH overtone vibration on $\text{Yb}^{3+} 2F_{5/2}$ and

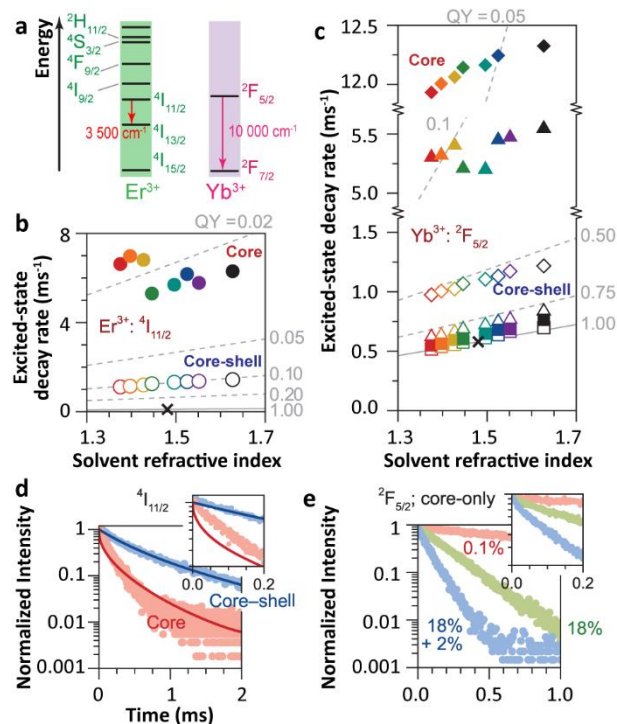


Fig. 10 (a) Energy diagram of Er^{3+} and Yb^{3+} ions. Averaged decay rates of the (b) $4I_{11/2}$ (Er^{3+}) of Er^{3+} single-doped $\beta\text{-NaYF}_4$ NPs and (c) $2F_{5/2}$ (Yb^{3+}) states of Yb^{3+} single-doped (squares, 0.1% Yb^{3+} ; triangles, 18% Yb^{3+}) and $\text{Er}^{3+}/\text{Yb}^{3+}$ co-doped (diamonds) $\beta\text{-NaYF}_4$ NPs with core-only and core-shell geometries in the different solvents shown in Fig. 9a (note the previously defined color code). The dashed lines represented the simulated curves. Decay curves of the (d) $4I_{11/2}$ and (e) $2F_{5/2}$ energy levels in core-only and core-shell UCNPs when dispersing in toluene (points) and the corresponding simulation results (lines). The insets show a zoom in the first 0.2 ms period. Adapted with permission from ref. ³⁵. Copyright (2018) American Chemical Society.

$\text{Er}^{3+} 4\text{I}_{13/2}$ states induced the huge luminescence dissipation in $\beta\text{-NaYF}_4\text{:18\%Yb}^{3+}$ and $\beta\text{-NaYF}_4\text{:20\%Er}^{3+}$ NPs, respectively. Thus, they speculated that the quenching effect of the CH 2-overtone vibration of the organic molecule on the $\text{Yb}^{3+} 2\text{F}_{5/2}$ luminescence should be significant. Meijerink's group made responses to these doubts afterwards¹⁰² and claimed that the overtone vibration-induced quenching effect had already been considered in the model. They also confirmed that the quenching effect of the CH 2-overtone vibration on the $\text{Yb}^{3+} 2\text{F}_{5/2}$ luminescence was very limited in the diluted-doped (0.1% Yb^{3+}) NPs.

Later, Meijerink's group studied the quenching behaviours of Er^{3+} and Yb^{3+} luminescence in UCNPs when dispersing in solutions with different vibration modes.¹⁰³ Two core-shell samples, $\beta\text{-NaYF}_4\text{:1\%Er}^{3+}\text{@}\beta\text{-NaYF}_4$ and $\beta\text{-NaYF}_4\text{:1\%Yb}^{3+}\text{@}\beta\text{-NaYF}_4$ with almost identical diameters and three different solvents, cyclohexane, H_2O and D_2O were employed. A very strong quenching of the $\text{Er}^{3+} 4\text{I}_{11/2}$ luminescence was observed in H_2O (Fig. 11a) because of the resonant OH fundamental vibration with the $4\text{I}_{11/2}\rightarrow 4\text{I}_{13/2}$ energy gap. Meanwhile, significant but with almost equal degrees of $\text{Er}^{3+} 4\text{I}_{11/2}$ luminescence quenching were detected in other two solvents (in D_2O , the lifetime of $4\text{I}_{11/2}$ state decreases from 10.26 ms ($\tau_{\text{radiative}}$) to 2.59 ms; in cyclohexane, the lifetime of $4\text{I}_{11/2}$ state decreases from 8.54 ms ($\tau_{\text{radiative}}$) to 2.25 ms), which were expectantly caused by the 2-phonon relaxation in both cases. Huge luminescence quenching of $\text{Er}^{3+} 4\text{I}_{13/2}$ state was detected in H_2O , while no significant quenching was detected in other two solvents (Fig. 11b). Limited quenching of $\text{Yb}^{3+} 2\text{F}_{5/2}$ luminescence was detected in three different solvents (Fig. 11c). In addition, concentration-dependent decay dynamics of $\text{Yb}^{3+} 2\text{F}_{5/2}$ luminescence and the shell passivation effect were studied in the system as well (Fig. 11d-e).

Interpretation of solvent quenching effect

Research of Meijerink's group provides a valuable guidance to understand the quenching effect of H_2O molecule. An important viewpoint is that the solvent-induced luminescence quenching can be treated as a type of FRET process by dipole-dipole coupling¹⁰⁴, and the quenching efficiency can be quantified by three factors: (1) energy matching between the electronic transition of Ln^{3+} ions and the vibration of the solvent molecules, (2) the oscillator strengths of involved transitions and (3) the spatial distance. Similar treatment has been conceptually adopted to describe the quenching behaviours of Ln^{3+} -doped LaF_3 and LaPO_4 NPs¹⁰⁵ and other nanoscale systems.¹⁰⁶

The proposed model successfully described the quenching behaviour of $\text{Er}^{3+} 4\text{F}_{9/2}$ luminescence in the core-only 2% Er^{3+} -doped sample as considering the strong coupling between the $4\text{F}_{9/2}\rightarrow 4\text{I}_{9/2}$ relaxation and the CH vibration (Fig. 9g). However, concerns should be raised to consider the quenching behaviour of $\text{Er}^{3+} 4\text{S}_{3/2}$ luminescence as the doping concentration increased. Experimental results demonstrated that the contribution of cross-relaxation (CR) to the luminescence quenching of $\text{Er}^{3+} 4\text{F}_{9/2}$ state was negligible in the high-doped samples, while $\text{Er}^{3+} 4\text{S}_{3/2}$ luminescence was greatly suffered

because of the suitable CR channels.³⁵ Noteworthy, the decay curve of $4\text{S}_{3/2}$ luminescence in the core-only 2% Er^{3+} doped sample was only well-simulated in the initial period (Fig. 9d), and a faster decay than the simulation was observed afterwards. This decay derivation was largely eliminated after shell coating. Therefore, the authors stated that it was caused by the Er^{3+} -to- Er^{3+} energy migration-assisted solvent quenching effect. Yet this explanation needs to be reassessed. Considering the stronger coupling interaction of $4\text{F}_{9/2}\rightarrow 4\text{I}_{9/2}$ relaxation to the CH vibration, this additional energy migration-assisted quenching effect on $\text{Er}^{3+} 4\text{F}_{9/2}$ luminescence should be severer than that of the $4\text{S}_{3/2}$ luminescence, which did not accord with the results as shown in Fig. 9g. Therefore, we consider the existence of other surface-related quenching

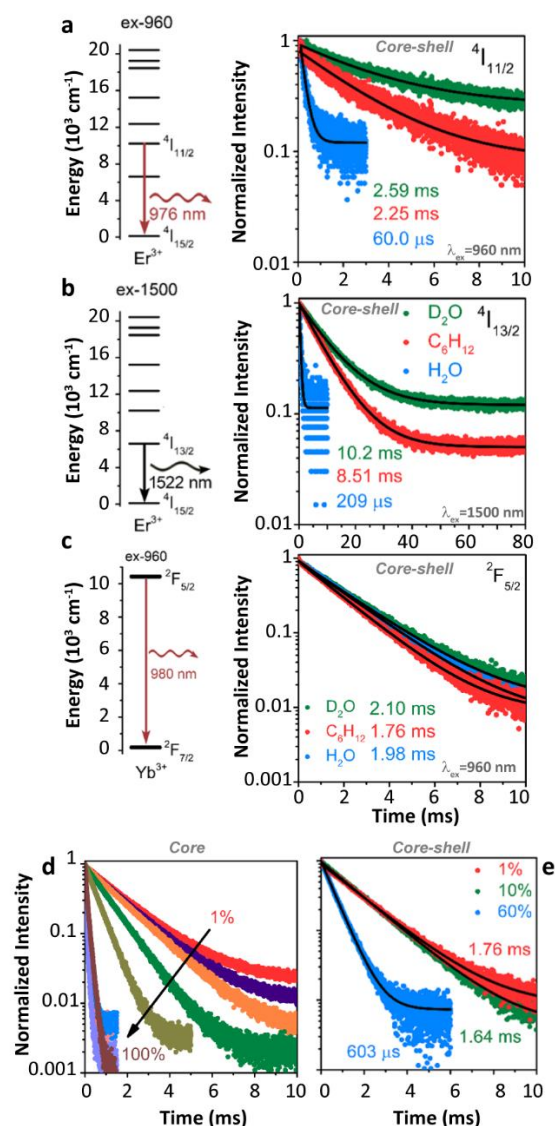


Fig. 11 (a, b) Energy diagrams of $\text{Er}^{3+} 4\text{I}_{11/2}$ and $4\text{I}_{13/2}$ states and the decay curves of $4\text{I}_{11/2}$ and $4\text{I}_{13/2}$ luminescence in $\beta\text{-NaYF}_4\text{:1\%Er}^{3+}\text{@}\beta\text{-NaYF}_4$ core-shell NPs dispersing in D_2O , cyclohexane and H_2O upon 960 nm and 1500 nm excitations, respectively. (c) Energy diagram of Yb^{3+} state and decay curves of $2\text{F}_{5/2}$ luminescence in $\beta\text{-NaYF}_4\text{:1\%Yb}^{3+}\text{@}\beta\text{-NaYF}_4$ core-shell NPs dispersing in different solvents. (d, e) Concentration-dependent decay curves of $\text{Yb}^{3+} 2\text{F}_{5/2}$ luminescence in Yb^{3+} single-doped $\beta\text{-NaYF}_4$ core-only and core-shell NPs as dispersing in cyclohexane upon 960 nm excitation, respectively. Adapted with permission from ref. ¹⁰³. Copyright (2018) American Chemical Society.

processes in the system, which results in the decay deviation as observed above.

The model deviation became more significant when simulating the luminescence decay of $\text{Er}^{3+} \ ^4\text{I}_{11/2}$ and $\text{Yb}^{3+} \ ^2\text{F}_{5/2}$ states. Massive luminescence quenching of $\text{Er}^{3+} \ ^4\text{I}_{11/2}$ state was observed, while the model could not reproduce the decay dynamics of $\ ^4\text{I}_{11/2}$ luminescence neither in core-only nor in core-shell samples (Fig. 10d), which indicated that the $\ ^4\text{I}_{11/2}$ luminescence was controlled by the other quenching effect. Moreover, the solvent quenching on $\text{Yb}^{3+} \ ^2\text{F}_{5/2}$ luminescence was supposed to be weak even considering the CH 2-overtone vibration (around 9000 cm^{-1}) in the system. The quenching of $\text{Yb}^{3+} \ ^2\text{F}_{5/2}$ luminescence was very limited in the very diluted-doped ($0.1\% \text{Yb}^{3+}$) core-only sample,¹⁰² while the quenching became noteworthy as Yb^{3+} concentration increased to 18% (Fig. 10c). As the solvent quenching effect was almost silent, the author believed that the uncoordinated Yb^{3+} on the particle surface should serve as the main quenching centre. However, careful consideration should be given to understand the detailed quenching pathway. On the one hand, the large $\ ^2\text{F}_{5/2} \rightarrow \ ^2\text{F}_{7/2}$ energy gap dismisses the possibility of phonon-assisted nonradiative relaxation in the system, especially in organic solutions without the participation of energetically favoured vibration models. On the other hand, several concentration-related processes can be active in the Yb^{3+} high-doped samples, especially the Yb^{3+} -to- Yb^{3+} energy migration.^{14, 84} With the assistance of this process, the averaged distance of excited Yb^{3+} to organic solvent molecule is shortened to some extents. Besides, the large number of Yb^{3+} in the sample directly increases the overall coupling degree of $\ ^2\text{F}_{5/2} \rightarrow \ ^2\text{F}_{7/2}$ relaxation to the organic solvent vibration in the system. These two factors cooperatively enhance the solvent quenching efficiency of $\text{Yb}^{3+} \ ^2\text{F}_{5/2}$ luminescence even if the energy matching condition is not satisfied. While the solvent quenching effect is still far enough to dominate the overall quenching of Yb^{3+} luminescence in the core-only high-doped sample dispersing in organic solvents, and the contribution of other surface-related quenching process should not be ignored.

The solvent quenching effect on the $\text{Er}^{3+} \ ^4\text{I}_{13/2}$ luminescence should be considered as well. Because of the relatively large $\ ^4\text{I}_{13/2} \rightarrow \ ^4\text{I}_{15/2}$ energy gap ($\sim 6800 \text{ cm}^{-1}$), the CH fundamental vibration-involved quenching effect on the $\ ^4\text{I}_{13/2}$ luminescence was less efficient than that on the luminescence of other Er^{3+} excited states in the diluted-doped sample (Fig. 11b).¹⁰⁷ Hence, some works studied the quenching efficiencies of overtone vibrations on the $\ ^4\text{I}_{13/2}$ luminescence (Fig. 12).¹⁰⁸⁻¹¹¹ Because of the suitable energy matching of the $\ ^4\text{I}_{13/2} \rightarrow \ ^4\text{I}_{15/2}$ relaxation to the OH 1-overtone vibration, a stronger quenching effect was expected. However, as Er^{3+} concentration increased, the efficient energy migration between different $\text{Er}^{3+} \ ^4\text{I}_{13/2}$ states was active, resulting in the decay acceleration of the $\ ^4\text{I}_{13/2}$ luminescence in the samples.¹⁰³

One thing that should be emphasized is that the above-mentioned quenching effect is only limited to the cases of single-doped samples, and the quenching mechanism becomes more complicated in co-doped samples.¹¹² For example, the

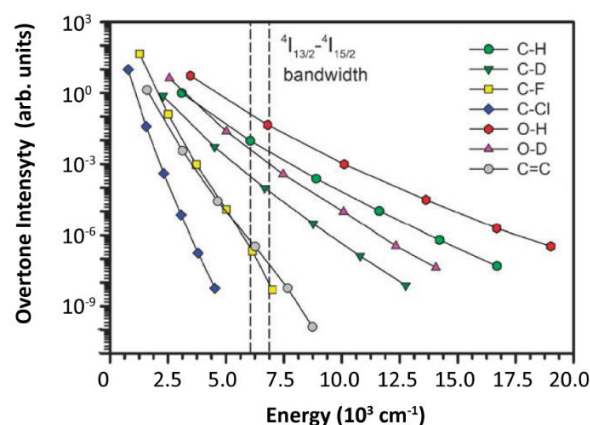


Fig. 12 Relative oscillator strength of different types of bonds normalized for the CH fundamental vibration. The $\ ^4\text{I}_{13/2} \rightarrow \ ^4\text{I}_{15/2}$ bandwidth of Er^{3+} was marked by two dashed lines in the figure. Reproduced from ref. ¹¹⁰ with permission from the Centre National de la Recherche Scientifique (CNRS) and The Royal Society of Chemistry.

solvent quenching effect on $\text{Yb}^{3+} \ ^2\text{F}_{5/2}$ luminescence was very limited in the Yb^{3+} diluted single-doped sample. While in the $\text{Yb}^{3+}/\text{Er}^{3+}$ co-doped system, the excitation energy of Yb^{3+} can “back-transfer” to Er^{3+} because of the nearly energy-resonant $\text{Er}^{3+} \ ^4\text{I}_{11/2}$ and $\text{Yb}^{3+} \ ^2\text{F}_{5/2}$ states and then rapidly dissipation.⁹³ This effect was more significant in Yb^{3+} high-doped samples (Fig. 10e). This synergistic process should be always kept in mind when studying the related issues.

A series of interesting results should be noticed. A gradual quenching relief was observed for $\text{Er}^{3+} \ ^4\text{S}_{3/2}$ luminescence when changing the solvent type from aliphatic to aromatic as shown in Fig. 9c and Fig. 13a. The corresponding CH fundamental

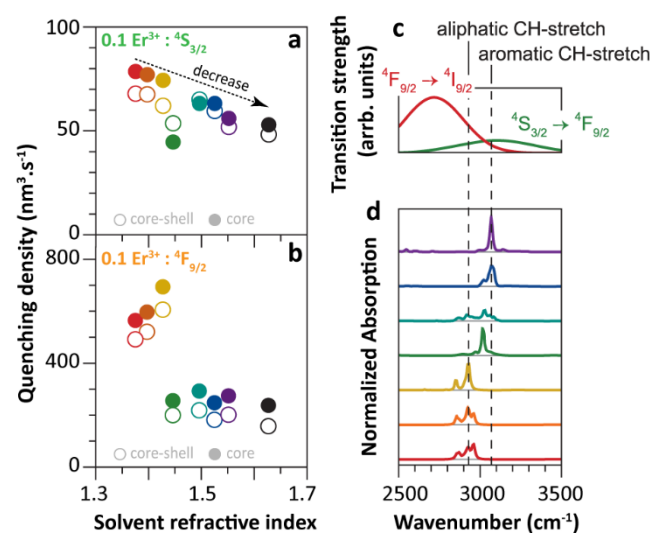


Fig. 13 (a, b) Solvent quenching densities deduced from model simulation results of the $\ ^4\text{S}_{3/2}$ and $\ ^4\text{F}_{9/2}$ luminescence in Er^{3+} diluted-doped $\beta\text{-NaYF}_4$ NPs with core-only and core-shell geometries dispersed in the different solvents shown in Fig. 9a (note the already defined color code). (c) The bandwidth of $\text{Er}^{3+} \ ^4\text{F}_{9/2} \rightarrow \ ^4\text{I}_{9/2}$ and $\ ^4\text{S}_{3/2} \rightarrow \ ^4\text{F}_{9/2}$ relaxations and (d) the solvent-dependent oscillator strengths and energies of the CH fundamental vibration modes. Adapted with permission from ref. ³⁵. Copyright (2018) American Chemical Society.

vibration energy increases with this variable sequence of organic solvent molecules and should gradually diminish the energy mismatching between $\text{Er}^{3+} \ ^4\text{S}_{3/2} \rightarrow \ ^4\text{F}_{9/2}$ relaxations and CH fundamental vibration (Fig. 13c-d). Similar quenching relief results were detected for $\text{Er}^{3+} \ ^4\text{I}_{11/2}$ and $\text{Yb}^{3+} \ ^2\text{F}_{5/2}$ luminescence as well (Fig. 10). In contrast, no solvent-dependent quenching relief was detected for $\text{Er}^{3+} \ ^4\text{S}_{9/2}$ luminescence (Fig. 13b) which its quenching behaviour was strongly dominated by the solvent quenching effect. Considering the energy matching is one of the dominant factors inducing the solvent quenching in the system, these quenching relief results indicate that the other quenching process, instead of solvent quenching, plays an essential role in controlling the quenching behaviours of these excited states. This process is active in the situation that the solvent quenching effect is not prominent, and probably raises a “shielding” effect which weakens the solvent quenching effect in the system.

Other surface-related effects

Most of the above-mentioned pending puzzles can be well solved by introducing other frequently mentioned surface-related quenching process.¹¹³ Because of the nature of wet synthesis of UCNPs with large SVR, many defects centres are created on the particle surface due to incomplete crystallization.¹¹⁴ Recent research demonstrated that these uncrystallized centres could be transferred to the ordered crystal structure after post-annealing treatment, resulting in several orders of magnitude UCL increase of UCNPs without a change in morphology.^{115, 116} (Fig. 14) Different from the random position of solvent molecule in the solution, these defects are localized on the particle surface generating an electrical dipole because of the imbalance of charge conservation in these regions. Besides the general-proposed irreversible electron-hole recombination-type quenching process induced by surface defects, the coupling interaction between electronic transition of Ln^{3+} and the assumed surface quenching dipole probably occurs as well, which raises the “surface-dipole quenching effect”. Such type of quenching process follows the FRET mechanism, and its quenching efficiency, is closely associated with (i) the separated distance between Ln^{3+} and surface defect, (ii) energy matching of involved transitions, and (iii) the corresponding oscillator strengths. Noted in this case that the overall coupling interaction is conceptualized as a point-to-plane ET form (r^{-4} relationship) provided that the particle surface were abstracted as a spherical plane,¹¹⁷⁻¹²⁰ which is different from the common r^{-6} relationship of point-to-point FRET form. This treatment is still under debate because some researchers believed that the nature of this interaction was attributed to the electron transfer and the exponential form relationship was more realistic.¹²¹ Phenomenologically, the assumed oscillator strength of surface-dipole is predicted to be feeble around 2800 cm^{-1} , moderate at 3200 cm^{-1} and large at 3500 cm^{-1} based on the results of the perfect model simulation of $\text{Er}^{3+} \ ^4\text{F}_{9/2}$ luminescence decay, the anomalous decay acceleration of $\text{Er}^{3+} \ ^4\text{S}_{3/2}$ luminescence in the later period, and the total deviation from the model of $\text{Er}^{3+} \ ^4\text{I}_{11/2} \rightarrow \ ^4\text{I}_{13/2}$ relaxation. As the Er^{3+}

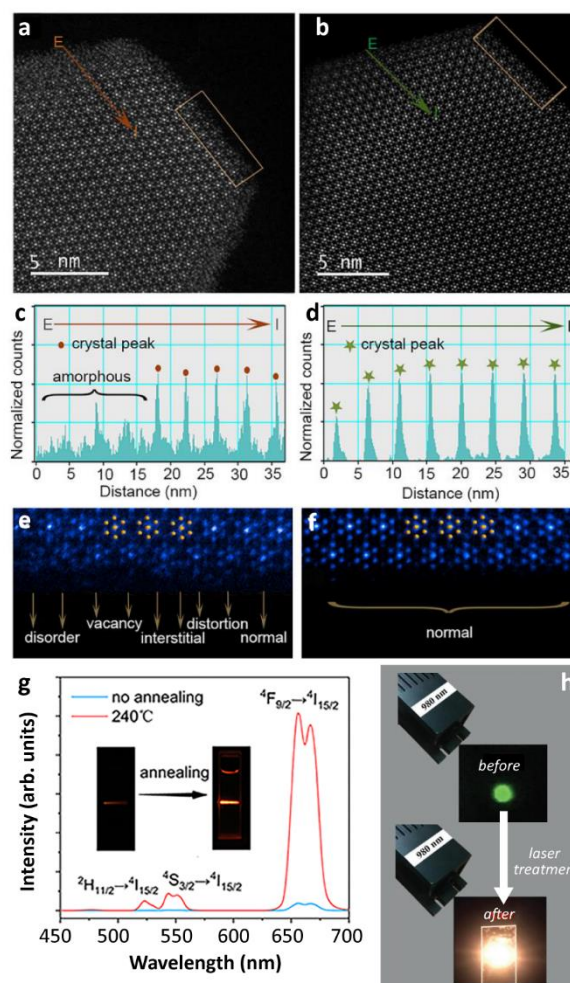


Fig. 14 (a, b) HAADF-STEM images, (c, d) intensity profiles as recorded by line scanning (directions of red and green arrows), and (e, f) enlarged crystal edge structure images of $\text{Yb}^{3+}/\text{Er}^{3+}$ co-doped KLu_2F_7 UCNPs before and after heating annealing. (g) UCL spectra of co-doped samples before and after annealing upon 980 nm excitation and the corresponding luminescence photographs. Reprinted with permission from ref. ¹¹⁵. Copyright (2018) American Chemical Society. (h) The photographs of $\text{Yb}^{3+}/\text{Er}^{3+}$ co-doped LuF_3 UCNPs upon 980 nm excitation before and after laser treatment. Adapted from ref. ¹¹⁶ with permission from the Wiley-VCH.

concentration increases, efficient Er^{3+} -to- Er^{3+} energy migration shortens the averaged distance between excited Ln^{3+} and surface defects, thus resulting in a more pronounced surface-dipole quenching effect on the Er^{3+} luminescence. Based on this hypothesis, surface-dipole quenching effect, instead of the solvent quenching effect, serves as the dominant role in controlling the luminescence quenching of $\text{Er}^{3+} \ ^4\text{I}_{11/2}$ state, which well-explains the reason of the significant but almost equal degrees of $\text{Er}^{3+} \ ^4\text{I}_{11/2}$ luminescence quenching as detected in D_2O and cyclohexene solutions with entirely different vibration energies. Besides, as the assumed surface-dipole gains a gradually increasing oscillator strength from 2800 to 3500 cm^{-1} , partly overlapped with the CH vibration energies of organic molecules, surface-dipoles will possibly couple with the CH vibration of solvent molecule and with excited Ln^{3+} , which results in the simultaneous weakening of solvent quenching and surface-dipole quenching effects to some extents and leads to the quenching relief of $\text{Er}^{3+} \ ^4\text{S}_{3/2}$ and $\ ^4\text{I}_{11/2}$ luminescence as

changing the solvent type from aliphatic to aromatic. In contrast, because of the absence of spectral overlapping between the surface-dipole transition and $\text{Er}^{3+} 4\text{F}_{9/2} \rightarrow 4\text{I}_{9/2}$ relaxation, no quenching relief is observed for $\text{Er}^{3+} 4\text{F}_{9/2}$ luminescence. Moreover, this surface-dipole quenching effect probably contributes to the significant luminescence quenching of $\text{Yb}^{3+} 2\text{F}_{5/2}$ state in the highly doped samples as well,¹²² and a systematic investigation should be done urgently in the future to identify its authenticity.

The situation is completely different by changing the solvent from an organic solution to H_2O . In consideration of the parity-forbidden nature of $\text{Ln}^{3+} 4f\text{-}4f$ transitions, the quenching efficiency of solvent quenching process largely depends on the oscillator strength of vibration mode of solvent molecule which is generally dipole-allowed.³⁵ Compared with the CH vibration of an organic molecule, the OH vibration in H_2O gains a larger oscillator strength, (Fig. 12) which induces stronger coupling interaction. Besides, most of the above-mentioned energy gaps of Er^{3+} can be exactly fulfilled by the OH fundamental vibration, such as $4\text{S}_{3/2} \rightarrow 4\text{F}_{9/2}$ (3200 cm^{-1}) and $4\text{I}_{11/2} \rightarrow 4\text{I}_{13/2}$ (3500 cm^{-1}).⁸⁶ Even for the large $\text{Er}^{3+} 4\text{I}_{13/2} \rightarrow 4\text{I}_{15/2}$ energy gap (6800 cm^{-1}), the quenching effect of the OH 1-overtone vibration is still efficient as verified experimentally¹²³ and theoretically.¹²⁴ One exception is the $\text{Er}^{3+} 4\text{F}_{9/2}$ state. Because of the large energy mismatch between $4\text{F}_{9/2} \rightarrow 4\text{I}_{9/2}$ gap and the OH fundamental vibration, the corresponding coupling interaction is almost negligible, leading to the H_2O -insensitivity of $4\text{F}_{9/2}$ luminescence, as previously observed.⁴⁷ Despite this, as the overall UCL efficiency depends on the individual electron population of different intermediated states, which all suffered from the OH vibration-induced solvent quenching effect, it is understandable that almost 99.9% UCL decrease has been detected in the core-only UCNP dispersed in H_2O .¹¹³ Special consideration should be given to comprehend the OH quenching effect on $\text{Yb}^{3+} 2\text{F}_{5/2}$ luminescence. Different from the CH 2-overtone vibration of the organic molecule, the OH 2-overtone vibration possesses more appropriate energy to fill the $\text{Yb}^{3+} 2\text{F}_{5/2} \rightarrow 2\text{F}_{7/2}$ energy gap, which gives rise to more efficient nonradiative relaxation of $\text{Yb}^{3+} 2\text{F}_{5/2}$ luminescence in H_2O . On the other hand, taking into consideration that the oscillator strength of the OH 2-overtone vibration is far weaker than that of the OH fundamental vibration,^{125, 126} the involved coupling interaction should not be very strong. The trade-off between these two factors largely determines the quenching efficiency of the OH vibration on $\text{Yb}^{3+} 2\text{F}_{5/2}$ luminescence in different diluted-doped systems. Other quenching processes will be active as Yb^{3+} concentration increases, which further complicates the quenching behaviour of $\text{Yb}^{3+} 2\text{F}_{5/2}$ luminescence. Great efforts should be made in the future to consummate the understanding on this crucial issue.

Inert-shell coating

Inert-shell coating serves as an effective way to weaken the solvent quenching effect in the system as previously described. In fact, inert-shell coating also provides the remarkable passivation effect to suppress the surface quenching effect on the luminescence of material with core-shell geometry. Almost

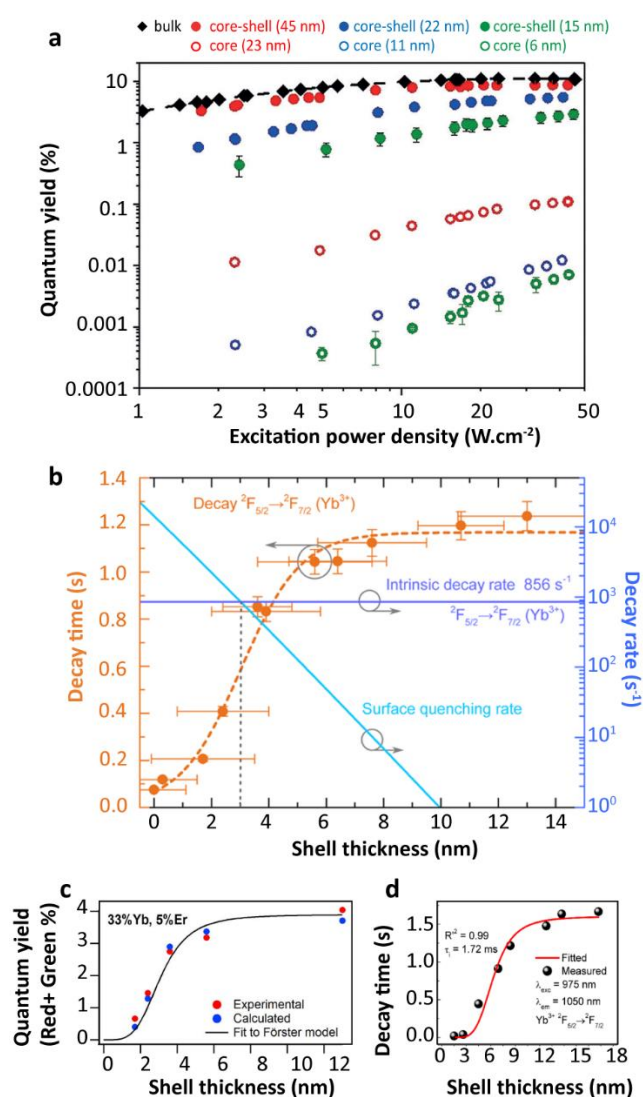


Fig. 15 (a) Excitation power density-dependent upconversion QY of $\text{Yb}^{3+}/\text{Er}^{3+}$ co-doped $\beta\text{-NaYF}_4$ core-only and core-shell UCNP with different diameters upon 980 nm excitation. Reproduced from ref. ²⁴ with permission from the Wiley-VCH. (b) Shell thickness-dependent decay time of $\text{Yb}^{3+} 2\text{F}_{5/2}$ luminescence in $\text{Yb}^{3+}/\text{Er}^{3+}$ co-doped $\beta\text{-NaYF}_4$ core-shell UCNP and the model simulation result (orange dash line). Reprinted with permission from ref. ¹²¹. Copyright (2016) American Chemical Society. (c) Shell thickness-dependent upconversion internal quantum efficiency values of $\text{Yb}^{3+}/\text{Er}^{3+}$ co-doped $\beta\text{-NaYF}_4$ core-shell UCNP and the model simulation result. Reprinted with permission from ref. ¹¹⁹. Copyright (2017) American Chemical Society. (d) Shell thickness-dependent decay time of $\text{Yb}^{3+} 2\text{F}_{5/2}$ luminescence in $\text{Yb}^{3+}/\text{Er}^{3+}$ co-doped $\beta\text{-NaGdF}_4$ core-shell UCNP and the model simulation result (red line). Reprinted with permission from ref. ⁵⁷. Copyright (2019) American Chemical Society.

one order of magnitude enhancement of Er^{3+} and Yb^{3+} infrared luminescence was observed after 3 nm thick inert-shell coating as well as a large enhancement of Er^{3+} visible luminescence.³⁵ (Fig. 10) Also, the enhancement degree was more significant in highly doped systems, and a two times larger enhancement of $\text{Er}^{3+} 4\text{S}_{3/2}$ luminescence was observed in 2% Er^{3+} than in 0.1% Er^{3+} single-doped samples. In fact, several orders of magnitude UCL enhancement were reported in samples after shell coating.¹²⁷⁻¹²⁹ As a representative example, Haase et al.²⁴ reported that the QY value of UCL of $\text{Yb}^{3+}/\text{Er}^{3+}$ co-doped UCNP (23 nm) increased from 0.01% to 9% after 11 nm thick inert-shell coating, which

was closed to the highest QY in the bulk sample (10.3%) ever reported. (Fig. 15a) Such passivation effect is significant for $\text{Yb}^{3+} {}^2\text{F}_{5/2}$ luminescence as well. Luminescence quenching of $\text{Yb}^{3+} {}^2\text{F}_{5/2}$ state was totally suppressed in the core-shell 10% Yb^{3+} single-doped NPs with 5 nm thick $\beta\text{-NaYF}_4$ inert-shell coating when dispersing in cyclohexane.¹⁰³ (Fig. 11e) More impressively, the OH quenching effect on $\text{Yb}^{3+} {}^2\text{F}_{5/2}$ luminescence was eliminated for core-shell 1% Yb^{3+} single-doped sample even dispersing in H_2O . (Fig. 11c) However, it is very confounded to entirely comprehend the role of inert-shell coating in the process of relieving surface quenching effect. The surface quenching effect is generally regarded as the generic term for substantial surface defect-related quenching processes complied with different quenching pathways (such as electron-hole recombination, multipole-multipole interaction, even including exchange interaction), and their individual contributions to the overall UCL quenching efficiency of UCNPs is rarely known. In addition, the spatial distance-dependent quenching efficiencies of these quenching processes should be highly diverse. Because of the localization of defects on the particle surface, the separated distance between excited Ln^{3+} and these quenching centres can be modified by adjusting the inert-shell thickness, which brings about distinct passivation degrees to different luminescence quenching processes of UCNPs. Together with other variables in the system, fully understanding and further controlling the shell passivation effect on UCL properties of the material with core-shell geometry is extremely difficult. Some attempts had been made to study this issue phenomenologically. Based on the results of Alivisatos's group¹²¹ (Fig. 15b) and Berry's group¹¹⁹ (Fig. 15c), the UCL quenching of $\text{Yb}^{3+}/\text{Er}^{3+}$ co-doped sample was efficiently suppressed with about 6 nm thick inert-shell coating, while Shao *et al.* believed that a far thicker inert-shell (~11 nm) was required.⁵⁷ (Fig. 15d) The validity of these statements is relative depending on specific sample treatments, experimental conditions, and data analysis criteria. Entirely different shell thickness will be required for absolutely passivating the surface quenching effect of different excited states because of the divergent distance dependences of interaction.¹²¹ Even under the conditions of identical apparatus and same type of NPs, the contributions from different quenching pathways to the luminescence quenching behaviour of a certain Ln^{3+} still needs to be cautiously interpreted.

Experimental reproducibility

Lack of criterion-normalized experimental data is regarded as the other apparent obstacle for the understanding of luminescence quenching mechanisms. In a typical setup, 808/980/1530 nm lasers are generally selected as the default and exclusive excitation sources to study the UCL properties of Ln^{3+} -doped UCNPs. However, the electron feeding kinetics of the intermediate state will have greatly influenced the luminescence decay dynamics of activator upon indirect excitation. Because of the relatively long lifetime of the intermediate state of the sensitizer, it is not possible to extract the intrinsic decay properties of excited states of activator and gain the meaningful insight into its special quenching behaviour.

Direct excitation by using different sources and wavelengths can be a suitable way to obtain the intrinsic luminescence decay kinetics of the studied state. However, some special cautions should be given to monitor the output stability of laser power density.⁹² A intermediate power density should be selected to avoid triggering other electron population processes.¹³⁰ The spatial distribution of power density on the excitation laser spot should be further optimized,¹³¹ especially for nonlinear UCL processes. Beyond that, more uncertainties in data are brought from the synthesis methodology of NPs. Completely different luminescence quenching behaviour of UCNPs can be induced by the fluctuation in any step during the materials synthesis, such as the choice of wet-reaction composition, synthesis procedure setup, and product post-treatment. Shao's group demonstrated that either the thermally enhanced or quenching UCL of UCNPs with identical core-shell geometry was obtained depending on different shell coating methods.⁵³ This could probably explain the reason why thermally enhanced UCL was still detected in the core-shell UCNPs as reported by Martínez *et al.*⁵⁵ and Xu's group.⁵⁰ Particle size and shell thickness of UCNPs, regarded as two of the most controllable variables, still cannot be accomplished as expected from batch-to-batch in practical terms.¹³²⁻¹³⁸ Moreover, recent results showed that the cation intermixing in UCNPs was significant,^{120, 139-142} resulting in the strong luminescence quenching through the deleterious CR processes between different Ln^{3+} , supposedly located in the core or shell regions.^{141, 143} In addition, the concern of cation dopant distributions in nanostructures was addressed frequently.^{142, 144-146} These issues not only perplex the detailed analysis of currently available results but also greatly prevent the explicit understanding of the overall quenching mechanism. Moreover, the precise record of experimental variables (such as the type of protective atmosphere using in the experimental chamber, relative humidity, sample pre-treatment method, equipment calibration procedures and relevant experimental parameters), is very important during the data collection process.¹³⁰ The absence of these information in the early works aiming at the topic of thermally enhanced UCL largely restricts the possibility of result reanalysis and data cross-check. In addition, reversibility should be carefully assessed. Despite that most researchers claimed that the phenomenon of thermally enhanced UCL was largely reversible in their investigations, some factors indeed resulted in the irreversible thermal enhancement of UCL.⁵⁶ For instance, local heat accumulation induced by continuous laser excitation has been proven to induce crystallization of the amorphous surface of NPs, which significantly enhanced the UCL intensity of studied samples.¹¹⁶ This effect is generally neglected during the successive spectral data collection. It is worth making the necessary efforts in the future to evaluate the contribution to the overall UCL enhancement of photothermally-induced surface structure transformation of the sample during the thermal cycling. This, and the careful reporting of experimental conditions, will facilitate the origin revealing of thermally enhanced UCL in the general cases.

Conclusions

Retrieving the topic of thermally enhanced UCL in UCNP, it is gradually realized that this phenomenon is attributed to concurrent effects of multiple factors. As one of the most dominants, the effect of moisture detachment is carefully discussed. Strong luminescence quenching of Ln³⁺-doped UCNP has been observed before when dispersing in aqueous solution, however the specific role of H₂O molecule in affecting the luminescence properties of material was rarely explored, which largely prevented the understanding of the experimental findings. In this work, the luminescence quenching of each excited state in the representative Yb³⁺/Er³⁺ co-doped UCNP is systematically interpreted based on the previously proposed solvent quenching model. The interaction between Ln³⁺ and H₂O molecule is carefully explicated. On the one hand, direct luminescence quenching of Yb³⁺ ²F_{5/2} state by the OH vibration is proved to be very limited in the diluted single-doped sample. On the other, the electron populations of most excited states of Er³⁺ are easily affected by H₂O molecule because of its suitable OH vibration energy, which probably results in a significant de-excitation of these states. As temperature increases, the adsorptive moisture gradually detaches from the particle surface, leading to a relief of the solvent quenching effect on Er³⁺ luminescence and inducing the UCL enhancement of the sample.

Different from the case of UCNP thoroughly dispersing in aqueous solution, the solvent quenching effect on the UCL generating from the surface-attached hydration layer of powder-formed NPs is relatively weaker when placed in the ambient atmosphere. In contrast, the quenching efficiencies of other processes on the luminescence of UCNP, possibly arising from the surface and intrinsic defect,¹²² is high and largely moisture-independent, generally leading to a very weak UCL of the sample at RT. On this occasion, the luminescence recovery caused by weakening the solvent quenching effect will be amplified to some extent, resulting in the observable UCL enhancement as temperature rises. Complete inert-shell coating is proven to effectively suppress the surface-related quenching effects and greatly preserve the UCL intensity of core Ln³⁺. Hence, in passivated core-shell UCNP the luminescence recovery gaining from the moisture detachment is insufficient to offset the intrinsic UCL quenching at high temperatures; therefore, thermal quenching behaviour is observed. More precisely, the thermal enhancement degree of UCL is associated with the extent of luminescence loss induced by various quenching effects beforehand. Therefore, it is understandable that many conflicting results have been reported because of the large uncertainty in data acquisition in different articles. Moreover, other factors, such as phase transition, thermal-induced line broadening, lattice expansion, as well as kinetic electron population of the intermediated state, should not be neglected. All these mechanisms contribute to the temperature-dependent luminescence properties of UCNP.

Many efforts should be further made to uncover the mystery of thermally enhanced UCL phenomenon. Lack of criterion-normalized experimental setup is regarded as one of the main

obstacles for the acquisition of cross-validated experimental results. Besides that, more uncertainties can be brought from the synthesis methodology of NPs. Future works should be proceeded to deeply understand the luminescence quenching mechanism in small-sized NPs on the foundation that the unity criteria of sample synthesis, experimental setup, and data analysis are regulated. Only with a fundamental understanding of quenching mechanisms will it be possible to develop UCNP with superior UCL properties, capable of meeting application requirements.

Conflicts of interest

There are no conflicts to declare.

Acknowledgements

The work was partially developed under the project CICECO-Aveiro Institute of Materials, UIDB/50011/2020 & UIDP/50011/2020, financed by Portuguese funds through the FCT/MEC and when appropriate co-financed by FEDER under the PT2020 Partnership Agreement. Financial support from the project NanoHeatControl, POCI-01-0145-FEDER-031469, funded by FEDER, through POCI and by Portuguese funds (OE), through FCT/MCTES, and by European Union's Horizon 2020 FET Open program under grant agreements no. 801305 are acknowledged. EDM acknowledges funding from National Agency for the Promotion of Science and Technology (ANPCyT), through grant PICT 2017-0307. R. S. would like to thank Dr. Zijun Wang (École Polytechnique) for valuable discussions.

References

1. F. Auzel, *Chem. Rev.*, 2004, **104**, 139-174.
2. F. Wang, Y. Han, C. S. Lim, Y. Lu, J. Wang, J. Xu, H. Chen, C. Zhang, M. Hong and X. Liu, *Nature*, 2010, **463**, 1061-1065.
3. J. Zhou, Q. Liu, W. Feng, Y. Sun and F. Li, *Chem. Rev.*, 2015, **115**, 395-465.
4. M. Bettinelli, L. Carlos and X. Liu, *Phys. Today*, 2015, **68**, 38.
5. M. Haase and H. Schäfer, *Angew. Chem. Int. Ed.*, 2011, **50**, 5808-5829.
6. P. A. Franken, A. E. Hill, C. W. Peters and G. Weinreich, *Phys. Rev. Lett.*, 1961, **7**, 118-119.
7. W. Kaiser and C. G. B. Garrett, *Phys. Rev. Lett.*, 1961, **7**, 229-231.
8. Y. Zhong, I. Rostami, Z. Wang, H. Dai and Z. Hu, *Adv. Mater.*, 2015, **27**, 6418-6422.
9. F. Auzel, *C. R. Acad. Sci.*, 1966, **262**, 1016-1019.
10. F. Auzel, *J. Lumin.*, 2020, **223**, 116900.
11. L. M. Wiesholler, F. Frenzel, B. Grauel, C. Würth, U. Resch-Genger and T. Hirsch, *Nanoscale*, 2019, **11**, 13440-13449.

12. G. Chen, H. Ågren, T. Y. Ohulchansky and P. N. Prasad, *Chem. Soc. Rev.*, 2015, **44**, 1680-1713.
13. X. Chen, D. Peng, Q. Ju and F. Wang, *Chem. Soc. Rev.*, 2015, **44**, 1318-1330.
14. Q. Su, S. Han, X. Xie, H. Zhu, H. Chen, C.-K. Chen, R.-S. Liu, X. Chen, F. Wang and X. Liu, *J. Am. Chem. Soc.*, 2012, **134**, 20849-20857.
15. F. Wang, R. Deng, J. Wang, Q. Wang, Y. Han, H. Zhu, X. Chen and X. Liu, *Nat. Mater.*, 2011, **10**, 968-973.
16. G. Chen, H. Qiu, P. N. Prasad and X. Chen, *Chem. Rev.*, 2014, **114**, 5161-5214.
17. Y. Lu, J. Zhao, R. Zhang, Y. Liu, D. Liu, E. M. Goldys, X. Yang, P. Xi, A. Sunna, J. Lu, Y. Shi, R. C. Leif, Y. Huo, J. Shen, J. A. Piper, J. P. Robinson and D. Jin, *Nat. Photonics*, 2014, **8**, 32-36.
18. R. Deng, F. Qin, R. Chen, W. Huang, M. Hong and X. Liu, *Nat. Nanotechnol.*, 2015, **10**, 237-242.
19. M. B. Prigozhin, P. C. Maurer, A. M. Courtis, N. Liu, M. D. Wisser, C. Siefe, B. Tian, E. Chan, G. Song, S. Fischer, S. Aloni, D. F. Ogletree, E. S. Barnard, L.-M. Joubert, J. Rao, A. P. Alivisatos, R. M. Macfarlane, B. E. Cohen, Y. Cui, J. A. Dionne and S. Chu, *Nat. Nanotechnol.*, 2019, **14**, 420-425.
20. C. D. S. Brites, X. Xie, M. L. Debasu, X. Qin, R. Chen, W. Huang, J. Rocha, X. Liu and L. D. Carlos, *Nat. Nanotechnol.*, 2016, **11**, 851-856.
21. D. J. Gargas, E. M. Chan, A. D. Ostrowski, S. Aloni, M. V. P. Altoe, E. S. Barnard, B. Sani, J. J. Urban, D. J. Milliron, B. E. Cohen and P. J. Schuck, *Nat. Nanotechnol.*, 2014, **9**, 300-305.
22. M. S. Meijer, P. A. Rojas-Gutierrez, D. Busko, I. A. Howard, F. Frenzel, C. Würth, U. Resch-Genger, B. S. Richards, A. Turshatov, J. A. Capobianco and S. Bonnet, *Phys. Chem. Chem. Phys.*, 2018, **20**, 22556-22562.
23. J.-C. Boyer and F. C. J. M. van Veggel, *Nanoscale*, 2010, **2**, 1417-1419.
24. C. Homann, L. Krukewitt, F. Frenzel, B. Grauel, C. Würth, U. Resch-Genger and M. Haase, *Angew. Chem., Int. Ed.*, 2018, **57**, 8765-8769.
25. E. D. Martínez, C. D. S. Brites, L. D. Carlos, R. R. Urbano and C. Rettori, *Front. Chem.*, 2019, **7**, 83.
26. B. Chen and F. Wang, *Trends Chem.*, 2020, **2**, 427-439.
27. Z. Wang, J. Christiansen, D. Wezendonk, X. Xie, M. A. van Huis and A. Meijerink, *Nanoscale*, 2019, **11**, 12188-12197.
28. J. Zhou, S. Wen, J. Liao, C. Clarke, S. A. Tawfik, W. Ren, C. Mi, F. Wang and D. Jin, *Nat. Photonics*, 2018, **12**, 154-158.
29. D. Li, Q. Shao, Y. Dong and J. Jiang, *J. Phys. Chem. C*, 2014, **118**, 22807-22813.
30. V. Bachmann, C. Ronda and A. Meijerink, *Chem. Mater.*, 2009, **21**, 2077-2084.
31. P. Dorenbos, *J. Phys.: Condens. Matter*, 2005, **17**, 8103-8111.
32. C. B. Layne, W. H. Lowdermilk and M. J. Weber, *Phys. Rev. B: Condens. Matter Mater. Phys.*, 1977, **16**, 10-20.
33. A. A. Setlur and J. J. Shiang, *J. Phys. Chem. C*, 2010, **114**, 2792-2798.
34. M. T. Berry and P. S. May, *J. Phys. Chem. A*, 2015, **119**, 9805-9811.
35. F. T. Rabouw, P. T. Prins, P. Villanueva-Delgado, M. Castelijns, R. G. Geitenbeek and A. Meijerink, *ACS Nano*, 2018, **12**, 4812-4823.
36. J. F. Suyver, J. Grimm, K. W. Krämer and H.-U. Güdel, *J. Lumin.*, 2005, **114**, 53-59.
37. W. Yu, W. Xu, H. Song and S. Zhang, *Dalton Trans.*, 2014, **43**, 6139-6147.
38. J. Zhao, H. Li, Q. Zeng, K. Song, X. Wang and X. Kong, *Chem. Lett.*, 2013, **42**, 310-312.
39. J. Shan, W. Kong, R. Wei, N. Yao and Y. Ju, *J. Appl. Phys.*, 2010, **107**, 054901.
40. J. Dong and J. I. Zink, *ACS Nano*, 2014, **8**, 5199-5207.
41. A. Bednarkiewicz, D. Wawrzynczyk, A. Gagor, L. Kepinski, M. Kurnatowska, L. Krajczyk, M. Nyk, M. Samoc and W. Strek, *Nanotechnology*, 2012, **23**, 145705.
42. G. K. Liu, H. Z. Zhuang and X. Y. Chen, *Nano Lett.*, 2002, **2**, 535-539.
43. G. K. Liu, X. Y. Chen, H. Z. Zhuang, S. Li and R. S. Niedbala, *J. Solid State Chem.*, 2003, **171**, 123-132.
44. D. D. Li, Q. Y. Shao, Y. Dong, F. Fang and J. Q. Jiang, *Part. Part. Syst. Charact.*, 2015, **32**, 728-733.
45. L. Tong, X. Li, R. Hua, T. Peng, Y. Wang, X. Zhang and B. Chen, *J. Nanosci. Nanotechnol.*, 2016, **16**, 816-821.

46. Q. Shao, G. Zhang, L. Ouyang, Y. Hu, Y. Dong and J. Jiang, *Nanoscale*, 2017, **9**, 12132-12141.
47. R. Arppe, I. Hyppänen, N. Perälä, R. Peltomaa, M. Kaiser, C. Würth, S. Christ, U. Resch-Genger, M. Schäferling and T. Soukka, *Nanoscale*, 2015, **7**, 11746-11757.
48. J. J. H. A. van Hest, G. A. Blab, H. C. Gerritsen, C. de Mello Donega and A. Meijerink, *J. Phys. Chem. C*, 2018, **122**, 3985-3993.
49. L. Liang and X. Liu, *Nat. Photonics*, 2018, **12**, 124-125.
50. L. Lei, D. Chen, C. Li, F. Huang, J. Zhang and S. Xu, *J. Mater. Chem. C*, 2018, **6**, 5427-5433.
51. J. Qiao, L. Ning, M. S. Molokeev, Y.-C. Chuang, Q. Liu and Z. Xia, *J. Am. Chem. Soc.*, 2018, **140**, 9730-9736.
52. R. Shi, L. Ning, Z. Wang, J. Chen, T.-K. Sham, Y. Huang, Z. Qi, C. Li, Q. Tang and H. Liang, *Adv. Opt. Mater.*, 2019, **7**, 1901187.
53. Y. Hu, Q. Shao, P. Zhang, Y. Dong, F. Fang and J. Jiang, *J. Phys. Chem. C*, 2018, **122**, 26142-26152.
54. L. Lei, J. Xia, Y. Cheng, Y. Wang, G. Bai, H. Xia and S. Xu, *J. Mater. Chem. C*, 2018, **6**, 11587-11592.
55. E. D. Martínez, C. D. S. Brites, L. D. Carlos, A. F. García-Flores, R. R. Urbano and C. Rettori, *Adv. Funct. Mater.*, 2019, **29**, 1807758.
56. D. Li, W. Wang, X. Liu, C. Jiang and J. Qiu, *J. Mater. Chem. C*, 2019, **7**, 4336-4343.
57. Y. Hu, Q. Shao, Y. Dong and J. Jiang, *J. Phys. Chem. C*, 2019, **123**, 22674-22679.
58. Q. Zou, P. Huang, W. Zheng, W. You, R. Li, D. Tu, J. Xu and X. Chen, *Nanoscale*, 2017, **9**, 6521-6528.
59. X. Cui, Y. Cheng, H. Lin, F. Huang, Q. Wu and Y. Wang, *Nanoscale*, 2017, **9**, 13794-13799.
60. J. Zuo, Q. Li, B. Xue, C. Li, Y. Chang, Y. Zhang, X. Liu, L. Tu, H. Zhang and X. Kong, *Nanoscale*, 2017, **9**, 7941-7946.
61. C. D. S. Brites, S. Balabhadra and L. D. Carlos, *Adv. Opt. Mater.*, 2019, **7**, 1801239.
62. C. D. S. Brites, A. Millán and L. D. Carlos, in *Handbook on the Physics and Chemistry of Rare Earths*, eds. J.-C. G. Bünzli and V. K. Pecharsky, Elsevier Science, B. V., Amsterdam, 2016, vol. 49, ch. 281, pp. 339-427.
63. L. D. Carlos and F. Palacio, *Thermometry at the nanoscale: Techniques and selected applications*, Royal Society of Chemistry, Oxfordshire, 2016.
64. M. Dramićanin, *Luminescence Thermometry: Methods, Materials, and Applications*, Elsevier, Cambridge, 2018.
65. D. Jaque and F. Vetrone, *Nanoscale*, 2012, **4**, 4301-4326.
66. Y. Cheng, Y. Gao, H. Lin, F. Huang and Y. Wang, *J. Mater. Chem. C*, 2018, **6**, 7462-7478.
67. C. Mi, J. Zhou, F. Wang, G. Lin and D. Jin, *Chem. Mater.*, 2019, **31**, 9480-9487.
68. Y. Hu, Q. Shao, X. Deng, S. Han, D. Song and J. Jiang, *Adv. Mater. Technol.*, 2019, **4**, 1800498.
69. D. Baek, T. K. Lee, I. Jeon, S. H. Joo, S. Shin, J. Park, S. J. Kang, S. K. Kwak and J. Lee, *Adv. Sci.*, 2020, **7**, 2000104. DOI: 10.1002/advs.202000104, 2000104.
70. C. D. S. Brites, E. D. Martínez, R. R. Urbano, C. Rettori and L. D. Carlos, *Front. Chem.*, 2019, **7**, 267.
71. Y. Hu, Q. Shao, X. Deng, D. Song, S. Han, Y. Dong and J. Jiang, *J. Mater. Chem. C*, 2019, **7**, 11770-11775.
72. H. Zou, X. Yang, B. Chen, Y. Du, B. Ren, X. Sun, X. Qiao, Q. Zhang and F. Wang, *Angew. Chem., Int. Ed.*, 2019, **58**, 17255-17259.
73. H. Zou, B. Chen, Y. Hu, Q. Zhang, X. Wang and F. Wang, *J. Phys. Chem. Lett.*, 2020, **11**, 3020-3024.
74. H. Hauser, B. Herter, C. L. M. Hofmann, O. Höhn, V. Kübler, S. Fischer, S. Wolf, S. Fasold, F. C. J. M. van Veggel, J. C. Goldschmidt and B. Bläsi, *Microelectron. Eng.*, 2018, **187-188**, 154-159.
75. W. J. Kim, M. Nyk and P. N. Prasad, *Nanotechnology*, 2009, **20**, 185301.
76. F. Kaboli, N. Ghazyani, M. Riahi, H. Zare-Behtash, M. H. Majles Ara and E. Heydari, *ACS Appl. Nano Mater.*, 2019, **2**, 3590-3596.
77. E. D. Martínez, R. R. Urbano and C. Rettori, *ACS Appl. Nano Mater.*, 2019, **2**, 6889-6897.
78. J.-C. Boyer, M.-P. Manseau, J. I. Murray and F. C. J. M. van Veggel, *Langmuir*, 2010, **26**, 1157-1164.
79. S. V. Eliseeva and J.-C. G. Bünzli, *Chem. Soc. Rev.*, 2010, **39**, 189-227.
80. S. Guo, X. Xie, L. Huang and W. Huang, *ACS Appl. Mater. Interfaces*, 2016, **8**, 847-853.
81. D. Toptygin, *J. Fluoresc.*, 2003, **13**, 201-219.

82. T. Senden, F. T. Rabouw and A. Meijerink, *ACS Nano*, 2015, **9**, 1801-1808.
83. C. K. Duan and M. F. Reid, *Spectrosc. Lett.*, 2007, **40**, 237-246.
84. S. Fischer, N. J. J. Johnson, J. Pichaandi, J. C. Goldschmidt and F. C. J. M. van Veggel, *J. Appl. Phys.*, 2015, **118**, 193105.
85. M. Kraft, C. Würth, V. Muhr, T. Hirsch and U. Resch-Genger, *Nano Res.*, 2018, **11**, 6360-6374.
86. C. Würth, M. Kaiser, S. Wilhelm, B. Grauel, T. Hirsch and U. Resch-Genger, *Nanoscale*, 2017, **9**, 4283-4294.
87. D. Yuan, M. C. Tan, R. E. Riman and G. M. Chow, *J. Phys. Chem. C*, 2013, **117**, 13297-13304.
88. M. C. Tan, G. A. Kumar, R. E. Riman, M. G. Brik, E. Brown and U. Hommerich, *J. Appl. Phys.*, 2009, **106**, 063118.
89. R. B. Anderson, S. J. Smith, P. S. May and M. T. Berry, *J. Phys. Chem. Lett.*, 2014, **5**, 36-42.
90. R. Martín-Rodríguez, F. T. Rabouw, M. Trevisani, M. Bettinelli and A. Meijerink, *Adv. Opt. Mater.*, 2015, **3**, 558-567.
91. H. Dong, L.-D. Sun and C.-H. Yan, *Chem. Soc. Rev.*, 2015, **44**, 1608-1634.
92. P. S. May and M. Berry, *Methods Appl. Fluoresc.*, 2019, **7**, 023001.
93. M. Kaiser, C. Würth, M. Kraft, T. Soukka and U. Resch-Genger, *Nano Res.*, 2019, **12**, 1871-1879.
94. I. Hyppänen, N. Höysniemi, R. Arppe, M. Schäferling and T. Soukka, *J. Phys. Chem. C*, 2017, **121**, 6924-6929.
95. G. Liu, *Chem. Soc. Rev.*, 2015, **44**, 1635-1652.
96. J. Zhao, Z. Lu, Y. Yin, C. McRae, J. A. Piper, J. M. Dawes, D. Jin and E. M. Goldys, *Nanoscale*, 2013, **5**, 944-952.
97. P. Villanueva-Delgado, D. Biner and K. W. Krämer, *J. Lumin.*, 2017, **189**, 84-90.
98. B. Huang, J. Bergstrand, S. Duan, Q. Zhan, J. Widengren, H. Ågren and H. Liu, *ACS Nano*, 2018, **12**, 10572-10575.
99. K. Huang, H. Liu, M. Kraft, S. Shikha, X. Zheng, H. Ågren, C. Würth, U. Resch-Genger and Y. Zhang, *Nanoscale*, 2018, **10**, 250-259.
100. E. S. Medvedev, *J. Chem. Phys.*, 2012, **137**, 174307.
101. K. K. Lehmann and A. M. Smith, *J. Chem. Phys.*, 1990, **93**, 6140-6147.
102. F. T. Rabouw, P. T. Prins, P. Villanueva-Delgado, M. Castelijns, R. G. Geitenbeek and A. Meijerink, *ACS Nano*, 2018, **12**, 10576-10577.
103. Z. Wang and A. Meijerink, *J. Phys. Chem. C*, 2018, **122**, 26298-26306.
104. J. M. F. van Dijk and M. F. H. Schuurmans, *J. Chem. Phys.*, 1983, **78**, 5317-5323.
105. J. W. Stouwdam, G. A. Hebbink, J. Huskens and F. C. J. M. van Veggel, *Chem. Mater.*, 2003, **15**, 4604-4616.
106. A. Aharoni, D. Oron, U. Banin, E. Rabani and J. Jortner, *Phys. Rev. Lett.*, 2008, **100**, 057404.
107. E. Kreidt, C. Kruck and M. Seitz, in *Handbook on the Physics and Chemistry of Rare Earths*, eds. J.-C. G. Bünzli and V. K. Pecharsky, Elsevier, 2018, vol. 53, pp. 35-79.
108. A. Monguzzi, M. I. Trioni, R. Tubino, A. Milani, L. Brambilla and C. Castiglioni, *Synth. Met.*, 2009, **159**, 2410-2412.
109. J. Scholten, G. A. Rosser, J. Wahsner, N. Alzakhem, C. Bischof, F. Stog, A. Beeby and M. Seitz, *J. Am. Chem. Soc.*, 2012, **134**, 13915-13917.
110. A. Monguzzi, A. Milani, L. Lodi, M. I. Trioni, R. Tubino and C. Castiglioni, *New J. Chem.*, 2009, **33**, 1542-1548.
111. Y. Yan, A. J. Faber and H. de Waal, *J. Non-Cryst. Solids*, 1995, **181**, 283-290.
112. N. J. J. Johnson, S. He, S. Diao, E. M. Chan, H. Dai and A. Almutairi, *J. Am. Chem. Soc.*, 2017, **139**, 3275-3282.
113. G. Tessitore, G. A. Mandl, M. G. Brik, W. Park and J. A. Capobianco, *Nanoscale*, 2019, **11**, 12015-12029.
114. R. Naccache, Q. Yu and J. A. Capobianco, *Adv. Opt. Mater.*, 2015, **3**, 482-509.
115. W. Bian, Y. Lin, T. Wang, X. Yu, J. Qiu, M. Zhou, H. Luo, S. F. Yu and X. Xu, *ACS Nano*, 2018, **12**, 3623-3628.
116. Q. Min, J. Lei, X. Guo, T. Wang, Q. Yang, D. Zhou, X. Yu, S. F. Yu, J. Qiu, Q. Zhan and X. Xu, *Adv. Funct. Mater.*, 2020, **30**, 1906137.
117. A. L. Rogach, T. A. Klar, J. M. Lupton, A. Meijerink and J. Feldmann, *J. Mater. Chem.*, 2009, **19**, 1208-1221.
118. H. Kuhn, *J. Chem. Phys.*, 1970, **53**, 101-108.

119. M. Y. Hossan, A. Hor, Q. Luu, S. J. Smith, P. S. May and M. T. Berry, *J. Phys. Chem. C*, 2017, **121**, 16592-16606.
120. C. Würth, S. Fischer, B. Grauel, A. P. Alivisatos and U. Resch-Genger, *J. Am. Chem. Soc.*, 2018, **140**, 4922-4928.
121. S. Fischer, N. D. Bronstein, J. K. Swabeck, E. M. Chan and A. P. Alivisatos, *Nano Lett.*, 2016, **16**, 7241-7247.
122. X. Qin, L. Shen, L. Liang, S. Han, Z. Yi and X. Liu, *J. Phys. Chem. C*, 2019, **123**, 11151-11161.
123. Y. Chun-Lei, D. Shi-Xun, Z. Gang, Z. Jun-Jie, H. Li-Li and J. Zhong-Hong, *Chin. Phys. Lett.*, 2005, **22**, 2926.
124. L. Ning, L. Lodi, M. I. Trioni, R. Tubino, S. Edvardsson and G. P. Brivio, *J. Phys.: Condens. Matter*, 2006, **19**, 016202.
125. T. Salmi, H. G. Kjaergaard and L. Halonen, *J. Phys. Chem. A*, 2009, **113**, 9124-9132.
126. T. Salmi, V. Hänninen, A. L. Garden, H. G. Kjaergaard, J. Tennyson and L. Halonen, *J. Phys. Chem. A*, 2012, **116**, 796-797.
127. F. Wang, J. Wang and X. Liu, *Angew. Chem. Int. Ed.*, 2010, **49**, 7456-7460.
128. Y. Zhong, G. Tian, Z. Gu, Y. Yang, L. Gu, Y. Zhao, Y. Ma and J. Yao, *Adv. Mater.*, 2014, **26**, 2831-2837.
129. S. Fischer, R. D. Mehlenbacher, A. Lay, C. Siefe, A. P. Alivisatos and J. A. Dionne, *Nano Lett.*, 2019, **19**, 3878-3885.
130. M. Kaiser, C. Würth, M. Kraft, I. Hyppänen, T. Soukka and U. Resch-Genger, *Nanoscale*, 2017, **9**, 10051-10058.
131. M. Mousavi, B. Thomasson, M. Li, M. Kraft, C. Würth, U. Resch-Genger and S. Andersson-Engels, *Phys. Chem. Chem. Phys.*, 2017, **19**, 22016-22022.
132. T. Rinkel, J. Nordmann, A. N. Raj and M. Haase, *Nanoscale*, 2014, **6**, 14523-14530.
133. S. Dühnen, T. Rinkel and M. Haase, *Chem. Mater.*, 2015, **27**, 4033-4039.
134. P. B. May, J. D. Suter, P. S. May and M. T. Berry, *J. Phys. Chem. C*, 2016, **120**, 9482-9489.
135. H.-X. Mai, Y.-W. Zhang, L.-D. Sun and C.-H. Yan, *J. Phys. Chem. C*, 2007, **111**, 13730-13739.
136. N. J. J. Johnson, A. Korinek, C. Dong and F. C. J. M. van Veggel, *J. Am. Chem. Soc.*, 2012, **134**, 11068-11071.
137. B. Voss and M. Haase, *ACS Nano*, 2013, **7**, 11242-11254.
138. B. Amouroux, C. Roux, J.-D. Marty, M. Pasturel, A. Bouchet, M. Sliwa, O. Leroux, F. Gauffre and C. Coudret, *Inorg. Chem.*, 2019, **58**, 5082-5088.
139. S. Dühnen and M. Haase, *Chem. Mater.*, 2015, **27**, 8375-8386.
140. L. Liu, X. Li, Y. Fan, C. Wang, A. M. El-Toni, M. S. Alhoshan, D. Zhao and F. Zhang, *Chem. Mater.*, 2019, **31**, 5608-5615.
141. D. Hudry, I. A. Howard, R. Popescu, D. Gerthsen and B. S. Richards, *Adv. Mater.*, 2019, **31**, 1900623.
142. C. Dong, J. Pichaandi, T. Regier and F. C. J. M. van Veggel, *J. Phys. Chem. C*, 2011, **115**, 15950-15958.
143. D. Hudry, R. Popescu, D. Busko, M. Diaz-Lopez, M. Abeykoon, P. Bordet, D. Gerthsen, I. A. Howard and B. S. Richards, *J. Mater. Chem. C*, 2019, **7**, 1164-1172.
144. J. F. Suyver, R. Meester, J. J. Kelly and A. Meijerink, *J. Lumin.*, 2003, **102-103**, 182-188.
145. T. C. Droubay, T. C. Kaspar, B. P. Kaspar and S. A. Chambers, *Phys. Rev. B: Condens. Matter Mater. Phys.*, 2009, **79**, 075324.
146. A. Podhorodecki, B. Krajnik, L. W. Golacki, U. Kostiv, G. Pawlik, M. Kaczmarek and D. Horák, *Nanoscale*, 2018, **10**, 21186-21196.

Table 1. Summary of the observations on the thermally enhanced UCL and the corresponding interpretations reported by the distinct research groups sorted by chronological order.

Year	Observations	Interpretation	Ref.
2005	<ul style="list-style-type: none"> Increase of integrated photon flux of the Er³⁺ emissions (originated from the ⁴I_{13/2}, ⁴S_{3/2}, and ²H_{9/2} excited levels) in Yb³⁺/Er³⁺ co-doped β-NaYF₄ powder as the temperature increases from 10 to 100 K 	The preferable population of the slightly high energy ² F _{5/2} multiplet of Yb ³⁺ at high temperatures, resulting in a more efficient Yb ³⁺ -to-Er ³⁺ ET	36
2014-2015	<ul style="list-style-type: none"> Thermal enhancement of UCL above-RT in small-sized Yb³⁺/Ln³⁺ (Ln = Er³⁺, Ho³⁺, Tm³⁺) co-doped β-NaYF₄ NPs. Excluded the possible contributions of laser-induced recrystallization and thermal-enhanced excitation light absorptivity to the thermally enhanced UCL phenomena Detected a more significant UCL enhancement as the particle size decreases 	The thermally enhanced UCL was caused by overcoming the restricted phonon bottleneck effect at high temperatures.	29, 44
2016	<ul style="list-style-type: none"> Found that the UCL intensity of Er³⁺ showed a "decrease-first increase-later" tendency as temperature increased in 75 nm Yb³⁺/Er³⁺ co-doped α-NaYF₄ NPs, and a similar but rather weaker emission intensity variation reappeared upon subsequent heating. Observed the luminescence enhancement and the increase of decay time of Yb³⁺ ²F_{5/2}-²F_{7/2} transition as temperature increased in 10 nm Yb³⁺/Ln³⁺ (Ln³⁺ = Ho³⁺, Tm³⁺) co-doped β-NaGdF₄ NPs. Recorded the weak thermal quenching of Tm³⁺ UCL in the core-shell Yb³⁺/Tm³⁺ co-doped UCNPs with 3.5 nm thick inert-shell. Observed the weak thermal quenching of Tm³⁺ UCL of core-only Yb³⁺/Tm³⁺ sample when measuring in argon atmosphere or dispersing the NPs in 1-octadecene. 	<p>The increase in UCL intensity was induced by the "adsorption-desorption" process of a small amount of H₂O molecules and other organic solvent residuals on the particle surface.</p> <p>The suppression of the OH vibration-induced (originated in the H₂O molecules around NPs) de-excitation of Yb³⁺ ²F_{5/2} state at high temperatures was the main factor inducing the thermally enhanced UCL.</p>	45, 46
2017	<ul style="list-style-type: none"> Observed the thermally enhanced UCL of Tb³⁺ ⁵D₃ and ⁵D₄ states in Tb³⁺-doped LiYbF₄ UCNPs complying with "cooperative upconversion" mechanisms. Observed a reversible thermally enhanced UCL in Yb³⁺/Eu³⁺ co-doped β-NaGdF₄ UCNPs following the "cooperative upconversion" mechanisms. Emphasized the stronger absolute UCL intensity of large-sized NPs than that of small-sized NPs even at high temperatures. Detected a slight thermal-induced lattice expansion as temperature increased. 	<p>The temperature-induced increasing of the population of the high-energy Stark level of the Yb³⁺ ²F_{5/2} state, favoured the phonon-assisted cooperative upconversion process and resulted in a noteworthy UCL enhancement.</p> <p>The thermal-induced lattice expansion deactivated the energy migration efficiency and suppressed the surface-related quenching effect, leading to the more favourable Yb³⁺-to-activators ET and resulting in the thermally enhanced UCL.</p>	58, 59
2018	<ul style="list-style-type: none"> Found the significant thermal enhancement of Tm³⁺ UCL in the core-only Yb³⁺/Tm³⁺ UCNPs with high Yb³⁺ concentration, while the thermal quenching of Tm³⁺ UCL were detected in the samples either with core-shell geometry, or after annealing at high temperature or with the μm-size. 	An efficient ET process was achieved with the participation of "surface phonons" generated by the [Yb...O] chelation on the surface of UCNPs, and more "surface phonons" were created at high temperature and immediately coupled with Yb ³⁺ , then transferred the	28

- Detected that a decrease in the size of NPs resulted in a more pronounced UCL enhancement, and a 2000-fold increase in $\text{Tm}^{3+} \text{ } ^1\text{G}_4$ UCL intensity was recorded in the 9.7 nm-sized $\text{Yb}^{3+}/\text{Tm}^{3+}$ co-doped UCNPs at 453 K.

trapped energy to the Tm^{3+} excited state producing brighter UCL.

The essence of "surface phonon"-assisted enhancement mechanism was the level-broadening of $\text{Yb}^{3+} \text{ } ^2\text{F}_{5/2}$ state at high temperature, which reduced the energy mismatch between the 4f-4f transitions of Yb^{3+} and activators. 49
- Observed a reversible thermally enhanced UCL of Ln^{3+} ($\text{Ln}^{3+} = \text{Tm}^{3+}, \text{Ho}^{3+}, \text{Er}^{3+}$) in a new-type fluoride system (20 nm-sized $\text{Yb}^{3+}/\text{Ln}^{3+}$ co-doped Na_3ZrF_7 UCNPs).

The thermal-induced trapped electron release was the dominant process inducing the thermally enhanced UCL. 50
- Detected the UCL enhancement in the ligand-free and inert-shell coating samples.
- Presented an increase in both the luminescence intensities and the $\text{Yb}^{3+} \text{ } ^2\text{F}_{5/2}$ decay times accompany with the significant thermally enhanced UCL in small-sized $\text{Yb}^{3+}/\text{Ln}^{3+}$ ($\text{Ln}^{3+} = \text{Tm}^{3+}, \text{Ho}^{3+}, \text{Er}^{3+}$) co-doped UCNPs as temperature increased, which could not be well-explained by "surface phonon"-assisted enhancement mechanism.
- Showed that the temperature dependence of UCL intensity of sample was closely correlated to the measurement atmosphere and the thermally enhanced UCL was only observed in the atmosphere containing H_2O molecules.

The work provided more evidence supporting their previous understandings on this topic in 2017 and raised some questions on the "surface phonon"-assisted enhancement mechanism as proposed by Jin's group. 53
- Observed the luminescence thermal quenching of OA ligand-stabilized $\text{Yb}^{3+}/\text{Ln}^{3+}$ co-doped UCNPs in dry Ar, which could not be well-explained by "surface phonon"-assisted enhancement mechanism
- Emphasized that entirely different temperature dependence of UCL of core-shell sample could be obtained by employing different shell-coating methods.
- Obtained a more significant UCL enhancement at elevated temperature in the core-shell system by introducing the structural defect.

The UCL enhancement could be further strengthened exploiting the defects as excitation energy reservoirs through the inequivalence substitution. 54
- Observed the thermally enhanced UCL in $\text{Yb}^{3+}/\text{Ln}^{3+}$ ($\text{Ln}^{3+} = \text{Tm}^{3+}, \text{Er}^{3+}$) co-doped UCNPs with 2 nm inert-shell coating, and a larger UCL enhancement was detected by doping 20% Yb^{3+} into the shell.

The luminescence enhancement was associated with the incomplete core shielding and Yb^{3+} -to- Yb^{3+} energy migration in the system. 55
- 2019 • Detected a non-reversible thermally enhanced UCL in core-only $\text{Yb}^{3+}/\text{Tm}^{3+}$ β - NaGdF_4 UCNPs

The nanoparticle sintering process at high temperatures (>500 K) caused the irreversible thermal enhancement of UCL. 56
- Reported the thermally enhanced UCL in a non-fluoride host, $\text{Yb}^{3+}/\text{Ln}^{3+}$ ($\text{Ln}^{3+} = \text{Tm}^{3+}, \text{Ho}^{3+}, \text{Er}^{3+}$) co-doped $\text{NaY}(\text{WO}_4)_2$. Excluded the possible contributions of thermal-induced phase transition and particle coalescence to the thermally enhanced UCL.

The strong thermally enhanced UCL was ascribed to the removal of surface moisture as temperature increased. 27

- Showed that the temperature dependence of UCL intensity of sample was closely correlated to the measurement atmosphere.
- Found the slight increase of $\text{Yb}^{3+} \ ^2\text{F}_{5/2}$ decay rate in N_2 and the significant decrease of that in air as temperature increased in 49% Yb^{3+} doped NPs.
- Detected a tiny mass gain (0.5%) of NPs in the cooling phase when temperature dropped back to 370 K from high temperature by employing the thermogravimetric analysis, which was attributed to the moisture re-adsorption.
- Found that the thermally enhanced UCL in core-shell $\text{Yb}^{3+}/\text{Er}^{3+}$ doped $\beta\text{-NaGdF}_4$ NPs was only observed in the H_2O containing atmospheres
- Observed the shell thickness dependent UCL enhancement of core-shell UCNPs at elevated temperature.
- Derived the maximum coupling distance (~11 nm) of excited Yb^{3+} and the OH vibration of surface H_2O .

The direct coupling of $\text{Yb}^{3+} \ ^2\text{F}_{5/2}$ excited state to the OH overtone vibration of the H_2O molecule was mainly responsible for the significant UCL quenching in the system, and this effect would be largely eliminated at high temperatures, resulting in the thermally enhanced UCL.

57